POLITECNICO
MILANO 1863

RE.PUBLIC@POLIMI
Research Publications at Politecnico di Milano

Post-Print

This is the accepted version of:

A. Zanotti, D. Algarotti
Aerodynamic Interaction Between Tandem Overlapping Propellers in eVTOL Airplane Mode Flight Condition
Aerospace Science and Technology, Vol. 124, 2022, 107518 (19 pages)
doi:10.1016/j.ast.2022.107518

The final publication is available at https://doi.org/10.1016/j.ast.2022.107518

Access to the published version may require subscription.

When citing this work, cite the original published paper.

© 2022. This manuscript version is made available under the CC-BY-NC-ND 4.0 license
http://creativecommons.org/licenses/by-nc-nd/4.0/

Permanent link to this version
http://hdl.handle.net/11311/1209246

Aerodynamic Interaction between Tandem Overlapping Propellers in eVTOL Airplane Mode Flight Condition

Alex Zanotti[a,1,*], Davide Algarotti[a,2]

[a]*Politecnico di Milano, Dipartimento di Scienze e Tecnologie Aerospaziali, via La Masa 34, 20156, Milan, Italy*

Abstract

The architecture of new electric aircraft concepts (eVTOLs) for urban air mobility is typically characterised by multi-propellers in tandem configurations with different degrees of rotor disks overlapping. Consequently, the aerodynamic interaction between front propellers slipstream and rear propellers represents one of the key-phenomena which influenced the performance and design of these novel aircraft configurations. A wind tunnel campaign was performed to investigate the aerodynamic interaction between two propellers in tandem with particular focus to airplane mode flight condition of eVTOLs. A systematic series of tests, including thrust and torque measurements and stereoscopic Particle Image Velocimetry (PIV) surveys, were performed on two co-rotating propellers models. The axial distance was fxed during tests while the lateral separation distance was changed to evaluate the effects of aerodynamic interaction on propellers performance and flow field due to different propeller disks overlapping. Load measurements pointed out a remarkable loss of rear propeller thrust occurring when the degree of overlapping between rotors disks is increased. On the other hand,

*Corresponding author
Email address: Alex.Zanotti@polimi.it (Alex Zanotti)
[1]Assistant Professor
[2]M.Sc. Graduate

spectral analysis of measured loads signals showed a higher amount of thrust fluctuations amplitude occurring when the degree of overlapping between propeller disks is partial. Stereo PIV results provided insights on the effects of aerodynamic interaction on rear propeller inflow and wake flow physics. Moreover, numerical simulations performed using a mid-fidelity aerodynamic solver based on vortex particle method (VPM) provided enhanced insights to comprehend the interacting flow mechanisms between front propeller slipstream and rear propeller blades responsible for the detrimental effects observed on rear propeller performance.

Keywords: Aerodynamics, Wind Tunnel, Particle Image Velocimetry, Vortex Particle Method, eVTOL

Notation

CFD	Computational Fluid Dynamics
C_P	power coefficient, $= P/(\rho n^3 D^5) = Q/(\rho n^2 D^5)$
C_T	thrust coefficient $= T/(\rho n^2 D^4)$
D	propeller diameter [m]
eVTOL	electrical Vertical Take Off and Landing aircraft
J	advance ratio $= V_\infty/(nD)$
L_y	lateral distance between the propeller axis [m]
M_t	tip Mach number
n	rotational speed [rad/s]
P	propeller power, $= Qn$ [W]
Q	propeller torque [Nm]
Q_{crit}	Q-criterion
r	propeller blade radial coordinate
R	propeller blade radius [m]
Re_D	Reynolds number based on propeller diameter
T	propeller thrust [N]
u	freestream velocity component [m/s]
v	vertical velocity component [m/s]
w	out-of-plane velocity component [m/s]
UAM	Urban Air Mobility
VPM	Vortex Particle Method
V_∞	wind tunnel freestream velocity [m/s]
$X - Y - Z$	propeller reference system
(X_v, Y_v)	in-plane coordinate of tip vortices core
η	propulsive efficiency $= J(C_T/C_P)$
ψ	blade azimuthal angle [deg]
ρ	air density [kg/m^3]
θ	blade pitch angle at 75% of the rotor radius [deg]
$\|\omega\|$	vorticity magnitude [1/s]
ω_z	out-of-plane vorticity component [1/s]

1. Introduction

The great challenge to create a sustainable world involves also air transport. Indeed, in the next future the growth of metropolitan areas will provide a wide increase of urban traffic, thus having a great impact on pollution and gas emission. In addition to the great effort spent by automotive companies for an effective electrification of ground transport vehicles, the aeronautical world is also looking to the development of unconventional vertical take-off and landing (VTOL) aircraft based on electric distributed propulsion (eVTOLs) to be considered, in the next future, as a sustainable alternative to ground transportation in overcrowded metropolitan areas [1]. This futuristic vision opened the market of urban air mobility (UAM), thus, in recent years, a large number of startup companies as well as aerospace industry devoted their effort to the design of novel short-range VTOL aircraft for transportation in urban areas. Despite the architectures of these novel air vehicles are rather diverse, as described in recent literature works [2, 3] collecting the most promising configurations investigated for UAM purposes, the common feature that can be clearly distinguished is related to the use of multiple propellers, typically mounted on a single or dual lifting surface. Consequently, a critical aspect to be thoroughly investigated is to evaluate possible detrimental effects on performance, handling qualities and noise impact of these brand new aircraft concepts due to aerodynamic interaction between propellers. Considering typical layout of eVTOL aircraft [2, 3], two main kind of propeller-propeller aerodynamic interaction could occur, i.e. with adjacent propellers in side-by-side configuration (propeller disks lying on same plane) or with propellers disks lying on planes at a certain axial distance with a degree of overlapping between them. The latter type of aerodynamic interaction occurs, particularly, during airplane mode flight condition of eV-

TOLs characterised by two rows of propellers positioned on tandem lifting surfaces, as for instance in the Airbus Vahana aircraft [4] shown in Fig. 1. Indeed, in cruise flight condition, the fore propeller slipstream invests the rear propeller blades, thus affecting propellers performance. Consequently, the investigation of the effects of aerodynamic interaction between two overlapping propellers, hereafter defined in "tandem" configuration, represents an essential aspect to drive the design of eVTOL vehicles.

Figure 1: Aibus Vahana layout (courtesy of A^3 by Airbus LLC).

Generally speaking, the aerodynamic interaction between rotors was widely investigated in literature, with particular effort for helicopters configurations. Indeed, rotorcraft research literature considers several studies of the aerodynamic interaction between tandem, coaxial rotors and tiltrotors, mainly focused on hover flight condition (see for instance the works from Harris [5] and Ramasamy [6]). Nevertheless, findings from rotorcraft research were slightly applicable to the study of aerodynamic interaction between propellers typical of eVTOL configurations. Indeed, in helicopter configurations, the flow mechanisms involved in wakes interaction between tandem rotors in cruise flight conditions [7] are characterised by rotor disks attitude almost aligned with free-stream. Therefore, they quite differs from the ones occurring in tandem propellers interaction with rotor disks almost normal to free-stream.

Moreover, helicopters rotors are made by articulated high-aspect ratio blades with a quite low twist, while propellers blades are rigidly mounted to rotating hub and are characterised by a lower aspect ratio and a quite higher twist.

Aerodynamic interaction between rotors represent a key-aspect also in the study of compound helicopters configurations. In particular, very recent literature presents some studies of aerodynamic interactions occurring between the main rotor and propellers wakes for a high speed compound helicopter as the Airbus Racer (see for instance [8]). Indeed, for such configuration strong aerodynamic interactions between propellers and main rotor wake occur typically at low speeds, affecting aircraft performance and maneuverability.

The great interest regarding the development of new multi-propellers architectures in the field of drones and UAV made recent literature plenty of both numerical and experimental works concerning the study of rotor-rotor aerodynamic interactions, with higher effort particularly on coaxial rotors configurations in hover condition. To cite few examples, Shukla et al. [9] investigated aerodynamic interaction of two coaxial rotors, finding higher figure of merit provided by upper rotor due to swirl recovery. Moreover, Brazinskas et al. [10] performed an experimental activity aimed to evaluate the performance of two co-axial rotors with partially overlapped disks with low longitudinal distance between them.

Side-by-side rotors configurations were carefully studied for applications on UAV quadcopters configurations. Indeed, the numerical works by Yoon et al. [11] and by Ventura Diaz and Yoon [12] investigated performance and efficiency of such multi-rotor systems by means of high-fidelity CFD simulations. An experimental systematic study of two side-by-side propellers was performed by Zhou et al. [13] aimed to the investigation of the effect of lateral separation between small UAV propellers in hover condition. Similarly,

Shukla and Komerath [14] performed stereo PIV measurements to study the interacting wake of a side-by-side configuration made by two mini-drone rotors, again for hover condition. Moreover, aerodynamic interaction between side-by-side propellers reproducing an airplane distributed propulsion system in cruise flight condition was thoroughly investigated in the work by de Vries et al. [15]. Indeed, in this latter work wind tunnel tests were performed over three adjacent propellers models at different staggered positions to evaluate the changes in their performance, flow-field characteristics and noise production due to their mutual aerodynamic interactions.

Aerodynamic interaction between multi-propellers configurations represents also an interesting benchmark for the validation of numerical CFD tools. In particular, in recent years, rotorcraft industry and research dedicated a wide effort in the development of mid-fidelity aerodynamic solvers to be used for the preliminary design of novel innovative VTOL aircraft configurations [16, 17] or to investigate problems related to interactional flow physics typical of complex rotorcraft configurations, as tiltrotors and compounds helicopters [18, 19]. The use of vortex particle methods (VPM) for wake modelling [20, 21], implemented in some of these mid-fidelity solvers, opened a novel scenario for a faster and more accurate evaluation of aerodynamic performance of complex rotorcraft vehicles. Indeed, these VPM-based mid-fidelity numerical tools showed the capability to accurately evaluate the complex flow mechanisms involved in aerodynamic interactions between rotor wakes and bodies, while keeping low the computational effort required for simulations. Nevertheless, these solvers required a robust validation against experimental data, as done for instance by Alvarez and Ning [22, 23] that reproduced the side-by-side propellers experiment in hover by Zhou et al. [13] through a mid-fidelity VPM aerodynamic code finding a quite promising

agreement with numerical results in terms of both performance and flow field representation.

Despite literature review highlights a comprehensive effort dedicated to the investigation of rotor-rotor aerodynamic interaction, these studies are mainly aimed to helicopter applications or to side-by-side propellers in hover flight conditions. Consequently, there is a certain lack in literature of experimental activities aimed to gain knowledge about aerodynamic interactions between tandem propellers configurations typical of eVTOL aircraft in forward flight conditions. As a matter of fact, a single experimental work by Stokkermans et al. [24] was found in very recent literature that was aimed to the systematic study of two propellers in both tandem and side-by-side configurations in such flight condition. In particular, this work analysed the effects of both such kind of aerodynamic interactions on propeller performance by means of loads measurements and investigated the interacting flow mechanisms by PIV for side-by-side propellers configurations only, particularly considering vertical takeoff and first stage of transition.

Therefore, the activity described in the present article is aimed to improve knowledge about tandem propellers aerodynamic interactions by filling the lack related to the study of interacting flow mechanisms occurring in airplane mode flight condition of eVTOL aircraft. Indeed, a systematic series of wind tunnel tests were performed on two propeller models in tandem configuration by changing their lateral separation distance at fixed axial distance. Wind tunnel tests included loads measurements to evaluate, particularly, the effects on rear propeller performance provided by aerodynamic interaction of front propeller slipstream. Moreover, stereo PIV surveys were performed to accurately evaluate novel insights about interacting flow field between propellers wakes for a typical cruise flight condition of eVTOL aircraft in urban

environment. In addition to experimental activity, numerical simulations reproducing wind tunnel tests configurations were performed using the mid-fidelity aerodynamic solver DUST [17]. The numerical activity was aimed to provide additional insights with respect to PIV observations regarding the interacting flow mechanisms occurring for tandem propellers configurations. Numerical results were, indeed, useful to enhance the physical comprehension of the effects on rear propeller performance due to aerodynamic interactions with front propeller wake, considering different degrees of overlapping between propellers disks.

Moreover, one of the purposes of the present activity is to collect an experimental database over propellers with a free geometry to be considered as a suitable tool for scientific and industrial communities to validate multi-fidelity CFD tools and provide insights to guide preliminary design of novel eVTOLs architectures.

The paper is organized as follows. Section §2 provides the description of the experimental set up, including propeller models design, measurements techniques and definition of test configurations. Section §3 provides the description of the numerical model built in DUST for the simulations of the tandem propellers configurations in cruise tested in the wind tunnel. Section §4 presents the discussion of the main results obtained by both experiments and simulations. Conclusions are drawn in Sec. §5.

2. Experimental Set up

The experimental activity was performed at the *S. De Ponte* wind tunnel of Politecnico di Milano. The closed-loop wind tunnel has a 1 m $\times$ 1.5 m test section and can reach a maximum speed of 55 m/s with a turbulence level lower than 0.1%.

2.1. Propeller models design

Two propeller models were designed and manufactured for the wind tunnel test campaign. Figure 2 shows the design of the propeller model.

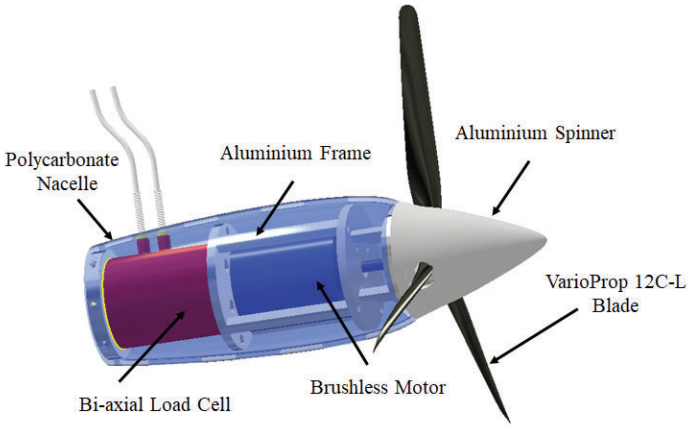

Figure 2: Layout of propeller model.

The propeller hub was designed using hobby-grade components. In particular, a three-bladed hub equipped with left-handed VarioProp 12C blades was used, thus resulting in a propeller disk diameter D equal to 300 mm. A 65 mm diameter aluminium spinner was screwed on the propeller hub. An internal aluminium frame was designed to support the propeller driving system and a bi-axial strain gauge load cell. The propeller was driven by a Scorpion brushless motor (5.3 kW continuous power) with shaft connected directly to propeller hub. The motor was powered by an external PWM-controlled electronic speed controller. A custom software developed in Labview was used to keep controlled both propellers at the desired rotational speed. A maximum fluctuation below 1% of the target rotational speed of the propellers was found during the wind tunnel tests. During the tests the blade azimuth phase of the two propellers blades were not synchronised. The accu-

rate control of propellers blade phase angles at the high RPM selected for the tests was not feasible due to hardware limitation of the hobby-grade external speed controller available for the tests. As a matter of fact, an accurate phase control of propellers blade represents a quite challenging issue for such kind of test set up and operating propellers conditions, particularly using hobby-grade electronic systems. Indeed, similar works described in literature do not use phase control of blade propellers in their experimental set up (see for instance [13, 24]). Nevertheless, in the present activity, numerical simulations allowed to evaluate additional information on the interactional flow physics of phase controlled propellers in tandem. A polycarbonate nacelle with 270 mm length was manufactured using FDM technique and mounted on the internal metallic frame to shield both the motor and the load cell. One of the propeller models was equipped with a Hall-effect sensor that was mounted on the metallic plate below the motor. The Hall-effect sensor was used during the tests to provide the 1/rev signal for the measurement of propeller rotational speed and to trigger the phase-locked PIV measurements.

2.2. Propeller models set up in the wind tunnel

The propeller models were mounted on metallic frames made by 30 mm $\times$ 30 mm squared section aluminium struts. A picture of the tandem propeller models set up inside the wind tunnel test section is shown in Fig. 3. A NACA 0025 airfoil shaped faring made by polystyrene was installed on the aluminium struts supporting the propellers. The motor cabling was embedded into the airfoil fairing to minimise aerodynamic interference during the tests. The two propellers were mounted in tandem configuration with an axial distance L_x between the propellers disk equal to 5 rotor radii. The aluminium strut attached to one of the lateral walls of the wind tunnel test section, acting as a rail, enabled to manually modify the lateral separation

distance between the models. In particular, the front propeller position was modified during the experimental campaign to allow tests with a different degree of overlapping between the tandem propellers disks. A thin stretched fabric bracing was used during the tests to stiffen both propellers support.

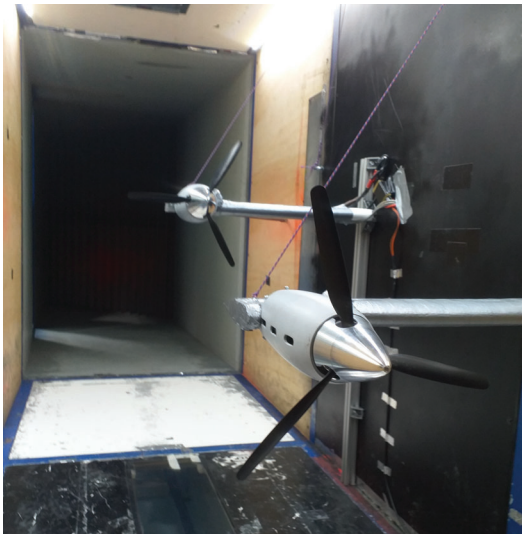

Figure 3: Layout of the tandem propeller models test set up at *S. De Ponte* wind tunnel.

2.3. Thrust and torque measurements set up

A Futek MBA500 strain gauge bi-axial load cell embedded in the internal metallic structure (see Fig. 2) was used to measure the propellers thrust and torque. The selected load cell has a F.S. range of ±222.4 N for thrust and of ±5.65 Nm for torque (non-linearity ±0.25% Rated Output, non-repeatability ±0.05% Rated Output). The load cell signals were acquired by a National Instrument c-DAQ system equipped with a strain/bridge NI 9237 module. The loads signals were sampled at 25 kHz and averaged over 10 seconds of acquisition time. Each test point was measured four times and 95% simultaneous confidence bands were calculated based on these four repetitions and plotted as errorbars on the performance curves comparison discussed in Sec.

4.1 to provide a clear indication of the measurement repeatability. The load cell employed in the measurements campaign showed quite good performance and high precision due to the two separate outputs for applied torque and thrust forces. In particular, for the single propeller configuration at advance ratio $J = 0.8$, representing the focus configuration investigated in the present work, a standard deviation of 0.5% of the averaged values of thrust and power coefficients was found over four repetitions. A quite slight degradation of the measurements performance was observed by increasing to twenty the number of repetitions for the same test configuration, as the standard deviation of both performance coefficients was found to be below 0.7% of their averaged values. Propellers loads and rotational speed were acquired simultaneously with wind tunnel parameters (i.e. dynamic pressure, air temperature, air relative humidity, atmospheric pressure) by a custom software developed using LabView to evaluate aerodynamic performance coefficients.

Wind tunnel wall corrections were applied to performance data. In particular, a solid blockage correction due to the airfoil shaped fairing and to nacelle encumbrance was considered following the methodology described in Barlow et al. [25]. Moreover, a slipstream correction to account for wind tunnel walls was considered following the methodology described by Glauert [26] and developed by Werle [27] to be applied to propellers aerodynamic coefficients. In the range of advance ratio tested, wall corrections provide a reduction of free-stream velocity below 1%, that was considered in the results comparison. In particular, at $J = 0.8$, representing the most investigated test condition in results discussion, a negligible reduction of 0.25% of free-stream velocity has to be considered due to wall corrections. The corrected free-stream velocity was used to evaluate aerodynamic loads coefficients and as well as to normalise the velocity measurements data.

2.4. Stereo PIV set up

The layout of PIV set up used for the wind tunnel tests is shown in Fig. 4. A Quantel Evergreen Nd:Yag double-pulse laser with an output energy of 200 mJ and wavelength of 532 nm was used for stereo PIV measurements. The laser was positioned under the plexiglass floor of wind tunnel test section to generate a laser sheet aligned with the longitudinal $X-Y$ mid-span plane by means of a 90° optic mirror. Two pairs of double-shutter cameras mounted on an external metallic structure around the test section were used to frame two different flow regions. In particular, two ILA.PIV.sCMOS cameras (Camera 1 and Camera 2 in Fig. 4) with a 16 bit 2560×2160 pixels array were arranged horizontally in stereoscopic mode to frame the wake flow region of the rear propeller in tandem (yellow box area in Fig. 4). Two Imperx ICL-B1921M CCD cameras (Camera 3 and Camera 4 in Fig. 4) with a 12-bit, 1952×1112 pixels array were arranged vertically to frame the inflow region of the rear propeller (green box area in Fig. 4).

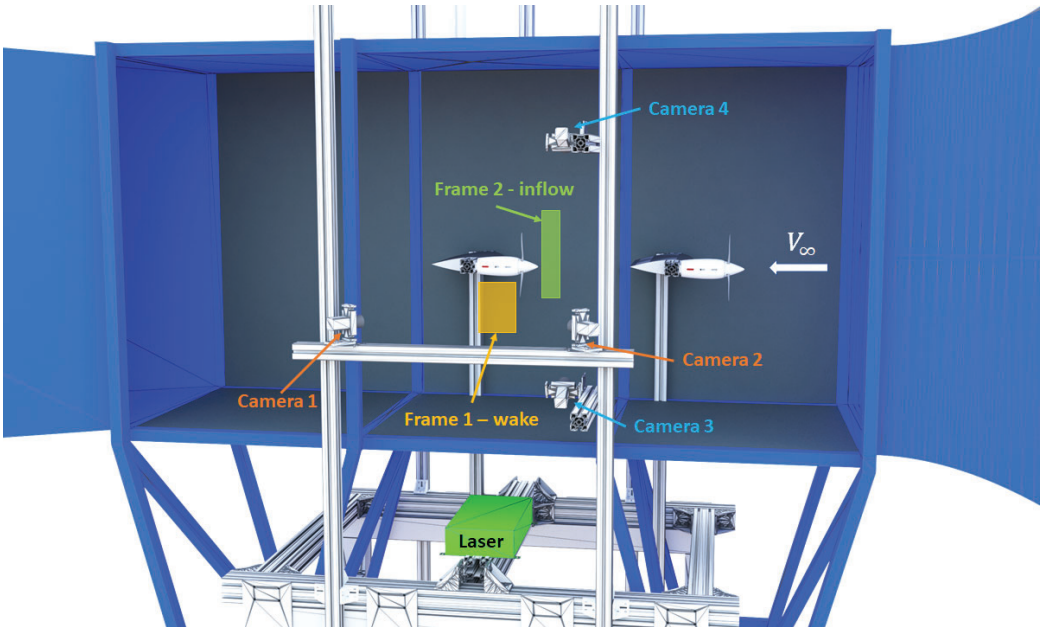

Figure 4: PIV set up for stereoscopic measurements on tandem propellers interaction at *S. De Ponte* wind tunnel.

During the whole test campaign the rear propeller was fixed with nacelle axis positioned at mid-span of test section height. Consequently, the cameras set up was not modified during tests with different overlapping between propellers disks, thus stereoscopic calibration was performed once. All the cameras were equipped with a 28 mm lens and tilting type lens for a correct focusing of the measurement window. The tilting lens mountings were adjusted in order to achieve the Scheimpflug condition [28]. The magnification factor was equal to 4.95 px/mm for both the measurement frames. The synchronization of the two laser pulses with the image pair exposure was controlled by a 6-channel Quantum Composer QC9618 pulse generator. Phase-locked and free-run 3C measurements were performed for each test configuration considered during the wind tunnel campaign (see Sec. 2.5). In particular, phase-locked measurements were performed with respect to

rear propeller blade azimuthal angle, by using the Hall-effect sensor signal mounted on rear model to trigger the laser pulses and the cameras images acquisition. As the phase angle between the tandem propellers blades was not synchronised, during phase locked measurements the front propeller was considered as in free-run condition, analogously to Zhou et al. experiments [13]. A particle generator (PIVpart30 by PIVTEC) equipped with Laskin atomizer nozzles was used to fulfill wind tunnel test section with seeding. The seeding particles consisted of small redDEHS droplets with a diameter in the range of 1–2 μm.

An amount of 500 image pairs for each test conditions was acquired during both phase-locked and free-rum measurements for the two investigated flow areas. The image pairs analysis was performed by using PIVview 3C software developed by PIVTEC. Post-processing made use of the multigrid interrogation method [28] starting from a 128 pixels $\times$ 128 pixels to a 16 pixels $\times$ 16 pixels interrogation window with effective 50% overlap. Thus, spatial resolution between adjacent measurement points resulted to be almost 1.6 mm for both the rear propeller inflow and wake surveys. Ensemble-averaged or phase-averaged flow fields obtained over the whole set of 500 image pairs acquired for each test condition are presented in the results discussion. The dimensions of the output areas of investigation were 70 mm $\times$ 336 mm high for the inflow survey and 190 mm $\times$ 282 mm for the wake flow survey. These fields of view dimensions were obtained by masking in post-processing phase the flow regions with outliers results due to propeller blades shadowing or to lack of laser energy. The accuracy of the PIV measurements can be estimated considering a maximum displacement error of 0.1 px [29]. Taking into account the pulse-separation time and the optical magnification used for the present tests, the maximum in-plane velocity error is below 1% of the

maximum in-plane velocity component, while a factor of $sqrt(2)$ higher can be considered for the out-of-plane velocity error [30].

2.5. Wind tunnel test conditions and configurations

Wind tunnel tests were aimed to study the aerodynamic interaction effects between two tandem propellers in forward flight with different degree of overlapping between the rotor disks. Figure 5 shows the layout of the two propellers in tandem configuration including the definitions of the axial (L_x) and lateral (L_y) separation distance between propellers.

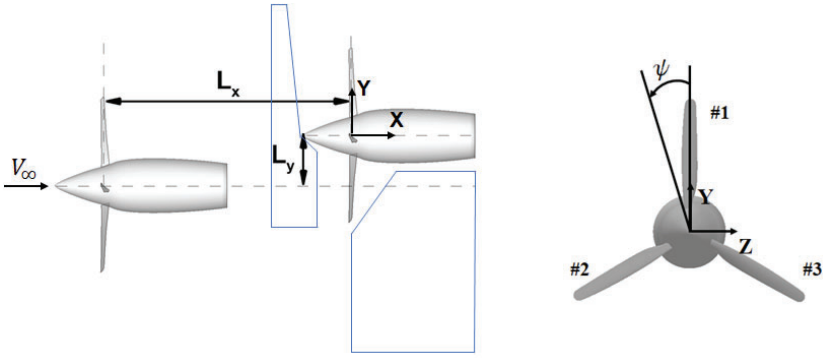

Figure 5: Layout of the tandem propellers configuration including separation distances (longitudinal distance not scaled); reference system definitions and PIV fields of view boundaries depicted by blue line (left), blade azimuthal angle definition (right).

In particular, L_x was defined as the longitudinal distance between tandem propellers disks, while L_y was defined as the lateral distance between londitudinal axis of the nacelle models. Moreover, the reference system $X - Y - Z$ used to present flow surveys results is defined in Fig. 5, where X axis is directed as wind tunnel freestream velocity direction (see Fig. 4) and the origin of the reference system is positioned on rear propeller disk center.

Wind tunnel test conditions consisted of runs performed with tandem co-rotating clockwise propellers with rotational speed of both propellers con-

trolled to 7050 RPM. This RPM target value was considered to reproduce a typical tip Mach number, i.e. $M_t = 0.325$, of full-scale eVTOL aircraft propellers in cruise flight condition [1, 31, 4]. Reynolds number based on propeller disk diameter and blade rotational velocity evaluated at 70%R corresponds to $Re_D = 1.96 \cdot 10^6$. Thus, since a 1:5 scale factor was used for propeller models diameter, wind tunnel tests were characterised by a lower Reynolds number with respect to a full-scale eVTOl aircraft like Airbus Vahana [4]. Nevertheless, such Reynolds number effects should not influence remarkably the main outcomes of the present experiments and consequently the main findings of the present work should be considered applicable to real aircraft flight configurations. During the tests, both propeller models rotational axis were aligned to wind tunnel free-stream velocity to reproduce eVTOLs cruise flight conditions. The blade pitch angle evaluated at $75\%R$ of both propellers models was fixed to $\theta = 26.5°$. Wind tunnel tests considered a single longitudinal separation distance between propeller disks, i.e. $L_x =$ 5R, corresponding almost to the separation distance between the two propellers rows of an Airbus Vahana like eVTOL aircraft. In order to evaluate the interactional effects provided by different degree of overlapping between propellers disks, wind tunnel tests included configurations with lateral distance $0 < L_y < 2R$. In particular, the front propeller model was moved downward while the rear propeller model remained fixed with nacelle axis aligned with test section centerline.

Performance measurements were performed covering an advance ratio range between $J = 0.4$, corresponding to wind tunnel free-stream velocity $V_\infty = 14.1$ m/s and $J = 1$, corresponding to $V_\infty = 35.2$ m/s, with step equal to 0.1. The advance ratio range selected for the tests was aimed to evaluate interactional effects from a moderate to a fast cruise flight speed of eVTOLs

aircraft in urban environment [2, 3]. Preliminary tests were performed over a single propeller (i.e. rear model) operating with same parameters to characterise the reference propeller performance for the evaluation of interactional effects by comparison with tandem propellers tests results. An overview of the test conditions and configurations for the performance measurements is reported in Tab. 1.

	RPM	θ [deg]	J	L_x/R	L_y/R
Single Prop	7050	26.5	[0.4 - 1] step 0.1	-	-
Tandem Props	7050	26.5	[0.4 - 1] step 0.1	5	[0, 0.5, 1, 1.5, 2]

Table 1: Overview of test conditions and configurations for performance measurements.

Stereo PIV surveys were performed for some selected test cases. In particular, PIV measurements were focused on a typical target cruise flight velocity of eVTOL aircraft in urban environment, i.e about 100 km per hour corresponding to $J = 0.8$. Three lateral separation distances, i.e. $L_y = 0$, 0.5 and 1, were considered for the flow surveys, as, due to the degree of overlapping between propellers disks, they represent the configurations that should be characterised by the highest aerodynamic interaction between front propeller slipstream and rear propeller disk. Moreover, as done for performance measurements, PIV surveys were also performed for the single propeller configuration at same test conditions. As previously stated, both free-run and phase-locked PIV surveys were performed during wind tunnel campaign. In particular, phase-locked measurements were performed for a single azimuthal angle of rear propeller #1 blade, i.e. $\psi = 170°$, as defined in Fig. 5 right. An overview of the test conditions and configurations for the for the stereo PIV measurements is reported in Tab. 2

	RPM	θ [deg]	J	L_x/R	L_y/R
Single Prop	7050	26.5	0.8	-	-
Tandem Props	7050	26.5	0.8	5	[0, 0.5, 1]

Table 2: Overview of test conditions and configurations for stereo PIV measurements.

3. Numerical simulations

Numerical simulations of the tandem propellers configurations investigated by experiments were performed to enhance the comprehension of the aerodynamic interactions effects on propeller performance and to provide additional insights to PIV surveys on interactional flow physics characterising such configurations. In particular, the mid-fidelity aerodynamic solver DUST, developed by Politecnico di Milano in collaboration with Airbus [17], was used for this numerical activity. The implementation of DUST exploits the Object Oriented paradigms of the latest Fortran standards to obtain the desired level of flexibility in modelling an aircraft potentially composed of several components and describing their motion. The aerodynamic solver relies on the Helmholtz decomposition of the velocity field, $\vec{u} = \vec{u}_\varphi + \vec{u}_\psi$, being $\vec{u}_\varphi$ and $\vec{u}_\psi$ the irrotational and solenoidal contributions respectively. The solution is advanced in time using a time-stepping algorithm that alternates the solution of a three-dimensional boundary element method for $\vec{u}_\varphi$ and the Lagrangian evolution in time of the rotational part of the velocity $\vec{u}_\psi$. Only the surface mesh of the model is required and different aerodynamic elements allow for different levels of fidelity in the model, ranging from lifting line elements [32, 33] to zero-thickness lifting surfaces and surface panels [34]. In particular, one-dimensional lifting line elements are used for a proper modelling of lifting bodies with high aspect ratio as blades. These elements naturally represent viscous effects, since they rely on tabulated aerodynamic

lift, drag and moment coefficients of two-dimensional sections as functions of the relative velocity direction and magnitude. This numerical tool, based on the use of VPM for wake modelling [20, 21], was thoroughly validated against experiments and high fidelity CFD over several rotorcraft configurations with increasing complexity, from simpler rotor-wing test cases [35], to a full tiltrotor [36] and a complete eVTOL vehicle as the Airbus Vahana aircraft [31]. Consequently, DUST can be considered in a mature state to be used for an accurate investigation of multi-rotors aerodynamic interactions. For the sake of consistency, the reader is referred to [17] for a complete description of the mathematical formulation of the code.

3.1. Numerical model of the propeller

The blade geometry used to built the numerical model of the propeller was digitally created by means of a 3D scanning of the blade model. In particular, a CAD software was used to generate the blade geometry from the surfaces provided by the scanning system. The maximum difference between the reconstructed blade CAD geometry and the 3D scanned surfaces was below 0.1 mm. A total number of 18 airfoil sections were extracted from the CAD geometry to evaluate twist, dihedral angle and chord distributions along the blade radial coordinate (r), as shown in Fig. 6. The propeller numerical model for DUST simulations was built using 40 lifting lines elements for each of the three blades. Table 3 shows the airfoils considered to build the blade numerical model and their distribution along span. In particular, the geometry of the two airfoils, i.e. R1 and R2, obtained from 3D blade scan and used to model the blade root region will be provided on request to authors.

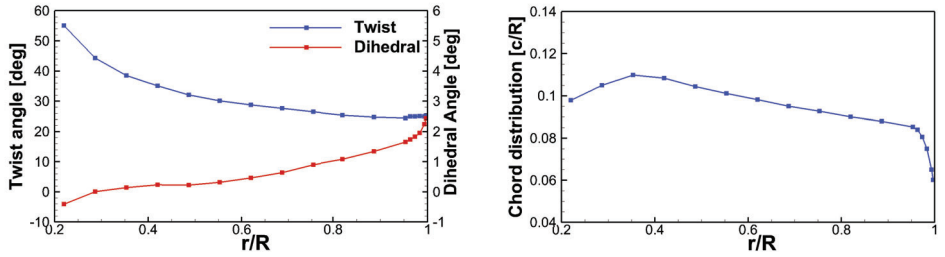

(a) (b)

Figure 6: Twist, dihedral angle and chord distributions of the propeller blade along span-wise radial coordinate.

Airfoil	Span-wise position [r/R]
R1	0 - 22%
R2	22% - 29%
GOE228	29% - 82%
GOE795	82% - 100%

Table 3: Airfoils sections with distribution along span used to build the propeller blade numerical model.

The mid and tip region of the blade was modelled using two airfoil from the Gottingen series, since from the scanning they resulted to be used for the design of these blade regions. The sectional tabulated aerodynamic coefficients of the root airfoil sections were calculated by XFOIL simulations [37] in the angle of attack range before stall. On the other hand, experimental data available in literature [38] were used for the Gottingen series airfoils. The Viterna method [39] was used to calculate the post-stall behaviour of the sectional aerodynamic loads coefficients in the range between $\pm 180°$ of angle of attack. In order to accurately reproduce the whole experimental propeller model geometry, the spinner-nacelle surface was included in the mesh. In particular, 1212 surface panel elements were used to model the

spinner-nacelle geometry, that will be also provided on request to authors. The layout of the propeller mesh built for DUST simulations is shown in Fig. 7.

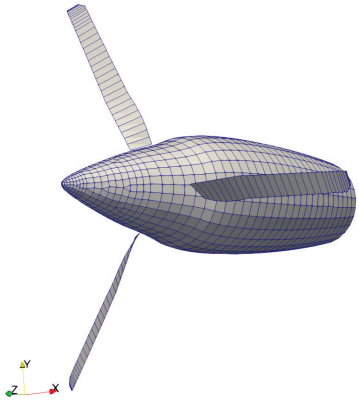

Figure 7: Layout of the propeller model mesh.

The numerical investigation was focused on cruise flight condition at advance ratio $J = 0.8$. Thus, numerical simulations reproduced the single and tandem propellers configurations tested during wind tunnel campaign for this advance ratio only (see Tab. 1). A spatial and time-dependence study was performed over the single propeller configuration at advance ratio $J = 0.8$, confirming the suitability of the spatial and time discretisations used to run the DUST simulations for such configurations. Moreover, a convergence study was also performed for the same test case with respect to the number of simulated propeller revolutions, showing converged values for propeller loads after three revolutions. Details about dependence and convergence studies were not here reported for the sake of consistency, but are available in Algarotti M.Sc. degree dissertation [40]. In particular, considering the results of these studies, all DUST simulations were performed considering a length of 8 propeller revolutions with a time discretisation of 5° of blade azimuthal angle. A fully developed wake for the interacting propellers test cases consisted

of around one million vortex particles. The computational time required to complete the simulation of a tandem propellers configuration was about 40 minutes using a workstation with a 18 cores processor.

4. Results and discussion

Numerical and experimental results will be discussed in the following sections to investigate two different aspects of the aerodynamic interaction between two overlapping propellers in tandem. Firstly, the effects of aerodynamic interaction on rear propeller performance will be presented by showing the experimental results obtained from thrust and torque measurements. Numerical simulations results will be discussed in parallel to provide a physical insight into the detrimental effects on performance observed by experiments. Secondly, a detailed insight about the interactional flow features that characterise the flow field around the tandem propellers will be provided by a parallel analysis of both PIV and numerical simulations results.

4.1. Propeller performance analysis

The performance of a single propeller, considered as reference to evaluate the effects of aerodynamic interaction between two overlapping propellers in tandem, is presented in Fig. 8 showing the behaviour of the measured thrust coefficient C_T, power coefficient C_P and propulsive efficiency η as a function of advance ratio J.

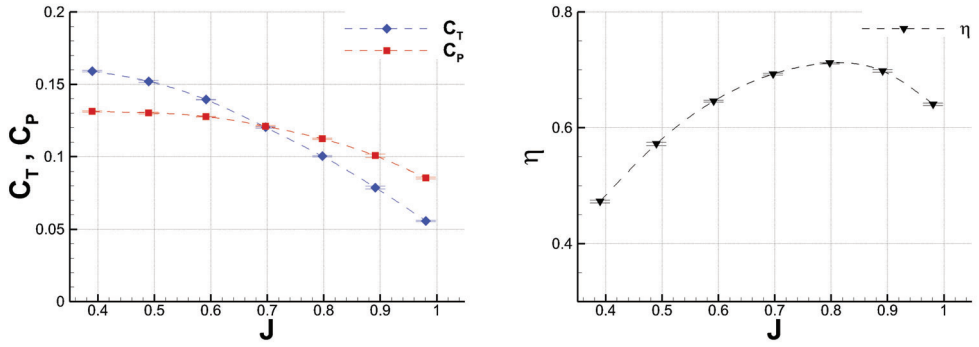

(a) (b)

Figure 8: Single propeller performance experimental results, $Re_D = 1.96 \cdot 10^6$, $M_t = 0.325$.

A very small errorbar can be observed in the whole range of the measured performance coefficients. The analysis of single propeller performance shows that, for the present test conditions, the propeller works at maximum efficiency in correspondence of $J = 0.8$, corresponding to a classical eVTOL cruise flight velocity (i.e. 100km/h) in urban areas, representing the target in this work. Then, thrust and torque measurements results obtained for overlapping tandem propellers configurations are discussed in the following. In particular, thrust and power coefficients measurements performed on the front propeller showed negligible differences for all the lateral separation distances L_y and the whole range of advance ratios considered during the tests. Indeed, a negligible effect is found on the front propeller by changing the degree of overlapping between propellers disks. Thus, performance measurements results obtained for the front propeller in tandem are not here presented for the sake of consistency.

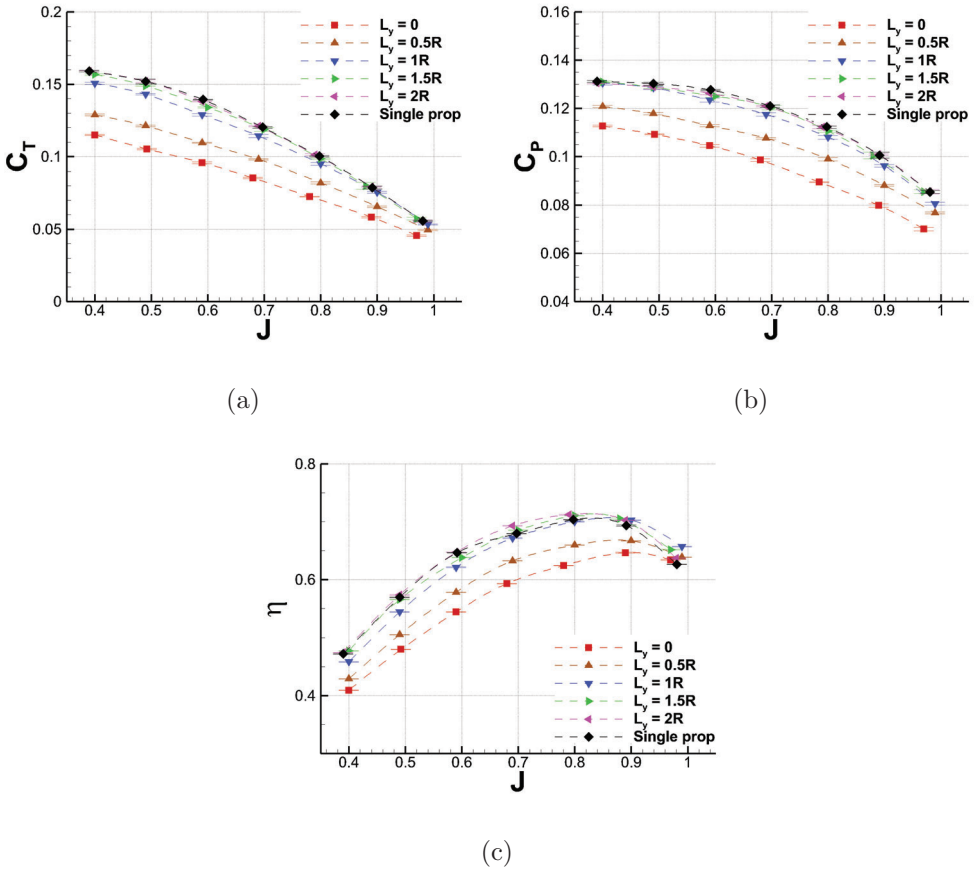

Figure 9: Comparison of the rear propeller experimental performance for tandem propellers configurations, $L_x = 5\text{R}$, $Re_D = 1.96 \cdot 10^6$, $M_t = 0.325$.

On the other hand, Fig. 9 shows the averaged thrust coefficient C_T, power coefficient and the propulsive efficiency η measured on rear propeller as a function of the advance ratio for the different lateral separation distance L_y considered during wind tunnel tests. The performance curves evaluated for single propeller configuration is plotted on the same graphs to behave as a reference for evaluating aerodynamic interaction effects on tandem propeller performance. As clearly visible from the curves comparison, a strong decrease of rear propeller performance occurs while reducing the lateral separation distance between propellers. This detrimental effect is observed for both thrust

and power coefficient in the whole range of advance ratios investigated during the tests. In particular, the highest loss of performance was observed when propellers disks are completely overlapped, i.e. $L_y = 0$. Indeed, for this configuration the front propeller slipstream invests the whole rear propeller disk, thus providing the highest interactional effects, as will be discussed in details by the following analysis of numerical simulations results. The aerodynamic interaction effect on rear propeller performance becomes negligible when the lateral separation distance is equal to the propellers disk diameter, i.e. $L_y =$ 2R. Indeed, for this configuration both thrust and power coefficients curves approach the single propeller one, as the rear propeller disk inflow is not influenced by front propeller slipstream. Moreover, the performance coefficients curves comparison shows apparently that the entity of rear propeller performance losses is not proportional to the lateral separation distance between the two propellers in tandem. Indeed, the higher rate of performance losses is found for lateral separation distances between $0 < L_y < 1R$. A quantitative evaluation of the rear propeller thrust and power losses with respect to single propeller configuration is provided respectively in Tabs. 4 and 5 for lateral separation distances $L_y = 0$, 0.5R and 1R, showing the more apparent effects of aerodynamic interaction, as will be later discussed. The present outcomes concerning rear propeller aerodynamic performance analysis are in agreement with the experimental results obtained by Stokkermans et al. [24] for similar test configurations. The propulsive efficiency curves comparison underlines that the highest detrimental effect on rear propeller performance occurs with complete overlap of the propeller disks. Moreover, the curves behaviour shows that in the range of disks overlap between $0 < L_y < 1R$, the peak of propulsive efficiency is shifted with respect to single propeller configuration, i.e to $J = 0.9$.

ΔC_T [%]	$J = 0.4$	$J = 0.5$	$J = 0.6$	$J = 0.7$	$J = 0.8$	$J = 0.9$	$J = 1$
$L_y = 0$	27.5	30.8	31.4	30.7	29.7	25.9	21.2
$L_y = 0.5$R	18.8	20.4	21.4	19.1	17.7	14.5	5.9
$L_y = 1$R	5	6.1	7.6	5.9	4.7	1.4	0.5

Table 4: Thrust coefficient losses ΔC_T [%] of the rear propeller in tandem with respect to single propeller configuration, $L_x = 5$R, $Re_D = 1.96 \cdot 10^6$, $M_t = 0.325$.

ΔC_P [%]	$J = 0.4$	$J = 0.5$	$J = 0.6$	$J = 0.7$	$J = 0.8$	$J = 0.9$	$J = 1$
$L_y = 0$	14	16.3	18.3	19.7	21.3	20.6	20.1
$L_y = 0.5$R	7.8	9.8	11.7	11.4	11.7	11.2	7.6
$L_y = 1$R	0.4	1.5	3.4	3.3	3.6	3.1	3.9

Table 5: Power coefficient losses ΔC_P [%] of the rear propeller in tandem with respect to single propeller configuration, $L_x = 5$R, $Re_D = 1.96 \cdot 10^6$, $M_t = 0.325$.

A more detailed analysis of aerodynamic interaction effects on rear propeller performance is provided for advance ratio $J = 0.8$, thanks to the availability of numerical simulations results obtained with DUST. Table 6 shows the comparison between experimental and numerical thrust and power coefficients evaluated for the single propeller configuration at $J = 0.8$.

	C_T	C_P
Experiment	0.101	0.107
DUST	0.1122	0.1136

Table 6: Comparison of the experimental and numerical aerodynamic performance of the single propeller at $J = 0.8$, $Re_D = 1.96 \cdot 10^6$, $M_t = 0.325$.

Figure 10 shows the comparison of thrust coefficient C_T and power coefficient C_P of rear propeller in tandem configuration evaluated by experiments

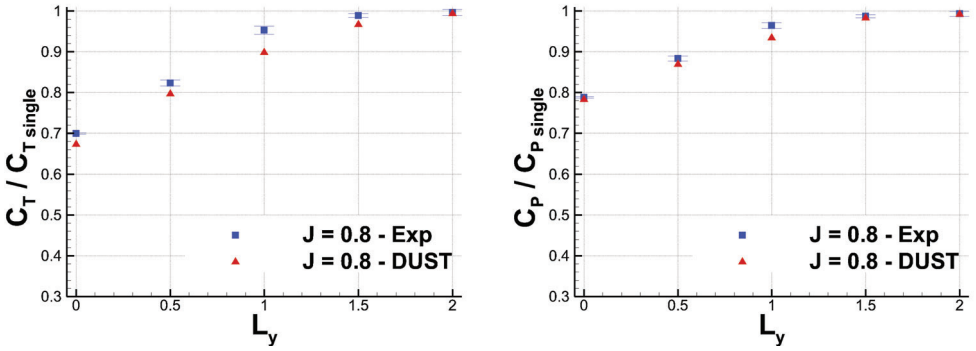

(a) (b)

Figure 10: Comparison of the rear propeller performance evaluated with experiments and numerical simulations for tandem propellers configurations at $J = 0.8$, $L_x = 5\text{R}$, $Re_D = 1.96 \cdot 10^6$, $M_t = 0.325$.

and numerical simulations at $J = 0.8$. In particular, numerical performance coefficients shown on the graphs were calculated as the average over the last three computed rotor revolutions and were normalised with respect to single propeller simulations values. Moreover, Fig. 10 reports the normalised confidence bands of experimental measurements evaluated as done in Fig. 8.

The normalised thrust and power coefficients approach unity for lateral separation distance $L_y = 2\text{R}$, confirming the negligible effects of aerodynamic interactions on propeller performance for such configuration. Increasing the degree of overlapping between propellers disks to $L_y = 1\text{R}$, the performance losses evaluated by experiments results to be quite small, i.e. in the order of few percents of the single propeller performance coefficients values. The performance losses result to be not proportional to the lateral separation distance. Indeed, the curves slope highly increases toward lateral distances between propellers lower than $L_y = 1\text{R}$, where aerodynamic interaction effects on rear propeller performance become more detrimental. In particular, experimental results obtained for co-axial propellers configuration show a

maximum loss of rear propeller performance of nearly 30% and 20% respectively for thrust and power coefficients (see Tabs. 4 and 5). Generally, the thrust coefficient reduction is larger with respect to power coefficient, thus indicating that at a certain thrust decrease corresponds a smaller power reduction and a consequent smaller reduction of fuel consumption.

The comparison between experimental and numerical normalised performance coefficients shows a quite good agreement in the whole range of lateral separation distance tested. Indeed, the maximum discrepancy between numerical and experimental data was found to be less than 5% and 3% respectively for thrust and power coefficients. In particular, these highest differences were found for the test configuration with $L_y = 1\text{R}$ that reflects, as will be later shown and discussed, the strongest aerodynamic interaction between propellers. Indeed, the largest discrepancy between numerical and experimental performance found at this lateral separation distance could be related to the strong aerodynamic interaction negatively affecting for this configuration the quality of loads measurements on rear propeller, as confirmed by the largest confidence band exposed by experimental measurements for this test condition. Moreover, the strong flow unsteadiness experienced by rear propeller for $L_y = 1\text{R}$ due to front propeller slipstream interaction is also confirmed by the time history of rear propeller thrust calculated by DUST and shown in Fig. 14(a). Nevertheless, the limited discrepancy observed between numerical and experimental results indicates that the numerical model can be considered suitable to describe this strong interactional aerodynamics problem. Indeed, in the following, numerical results are discussed to provide insights about the occurrence of detrimental effects on propeller performance for different degrees of overlapping between propellers disks. With this aim, the effects provided by the front propeller slipstream on rear propeller disk

inflow was investigated by analysing the distributions of axial velocity u_a, tangential velocity u_t, effective angle of attack α_{eff} and sectional lift coefficient C_l experienced by a rear propeller blade along the last rotor revolution computed by numerical simulations. In particular, these quantities were computed as variations with respect to single propeller simulations to highlight the effects due to front propeller aerodynamic interactions. Figures 11-13 shows these polar plots for the test cases with lateral distances $L_y = 0$, $L_y = 0.5$R and $L_y = 1$R, showing the greatest interaction effects on rear propeller aerodynamic performance. The polar plots colorbars range shown in Figs. 11-13 is kept constant for each variable in order to highlight the differences of these physical quantities obtained for the configurations with different degree of propellers disks overlapping.

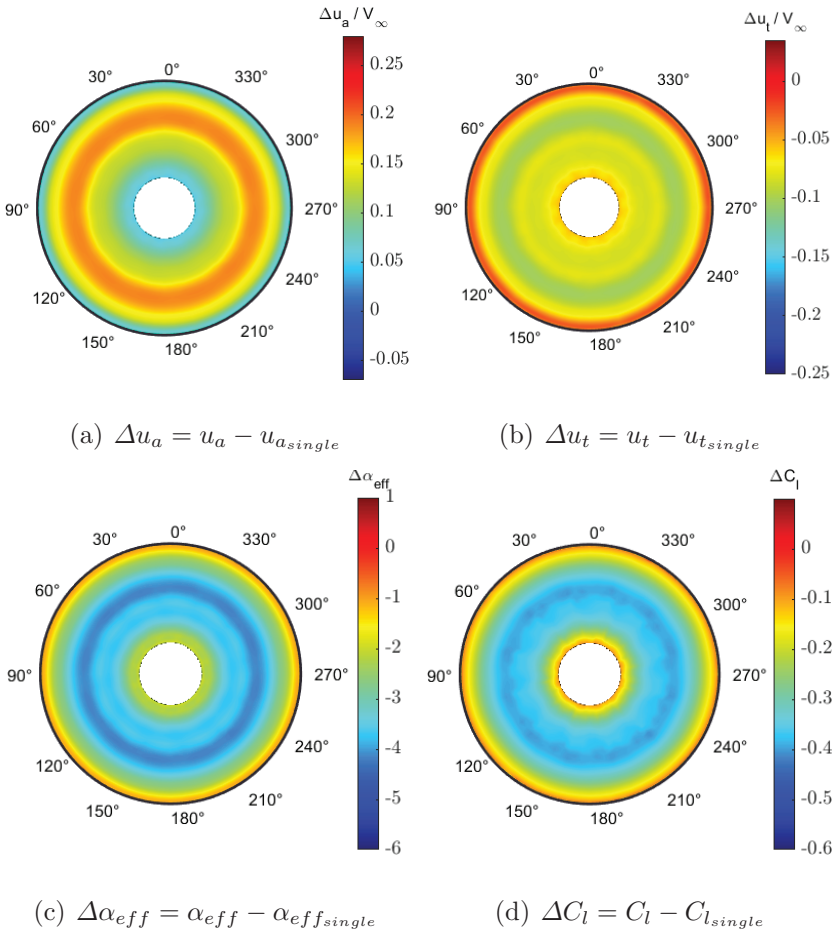

(a) $\Delta u_a = u_a - u_{a_{single}}$ (b) $\Delta u_t = u_t - u_{t_{single}}$

(c) $\Delta \alpha_{eff} = \alpha_{eff} - \alpha_{eff_{single}}$ (d) $\Delta C_l = C_l - C_{l_{single}}$

Figure 11: Variations of the axial velocity, tangential velocity, effective angle of attack and sectional lift coefficient computed by DUST simulations at $J = 0.8$ on the rear propeller blade in tandem configurations with respect to the single rotor configuration for the last rotor revolution, $L_x = 5\text{R}$, $L_y = 0$, $Re_D = 1.96 \cdot 10^6$, $M_t = 0.325$.

Numerical simulations results obtained for tandem propellers in co-axial configuration, i.e. $L_y = 0$ show a remarkable increase of the axial velocity component experienced by the outer portion of rear propeller blade due to the ingestion of front propeller slipstream (see Fig.11(a)). Moreover, a slight negative variation of tangential velocity can be observed on the same portion of rear propeller blade due to the interaction of front propeller slipstream (see Fig. 11(b)). The combination of these velocity components variations is

responsible of a consistent decrease of the local effective angle of attack and a consequent decrease of the sectional lift coefficient experienced by a large portion of rear propeller blade along span (see Figs. 11(c) and 11(d)). Thus, the present physical interpretation of numerical results enabled to explain the large performance loss in terms of average thrust observed for this co-axial configuration (see Fig.10).

Simulation results for $L_y = 0.5R$ clearly shows the footprint of the front propeller slipstream partially investing the rear propeller disk. In particular, an increase of axial velocity component combined with a lower decrease of tangential velocity component is experienced along almost the entire rear propeller blade span by the lower half portion of the propeller disk overlapped to the front propeller slipstream (see Figs.12(a) and 12(b)). Analogously to what observed for the configuration with $L_y = 0$, the combination of these velocity components variations provides a reduction of the effective angle of attack of rear propeller blade and a consequent decrease of sectional lift coefficient with respect to single propeller configuration. In particular, the thrust loss is observed over almost half of the propeller blade revolution, while blade performance remains almost unaltered with respect to single propeller configuration in the upper portion of rear propeller disk (see Figs. 12(c) and 12(d)).

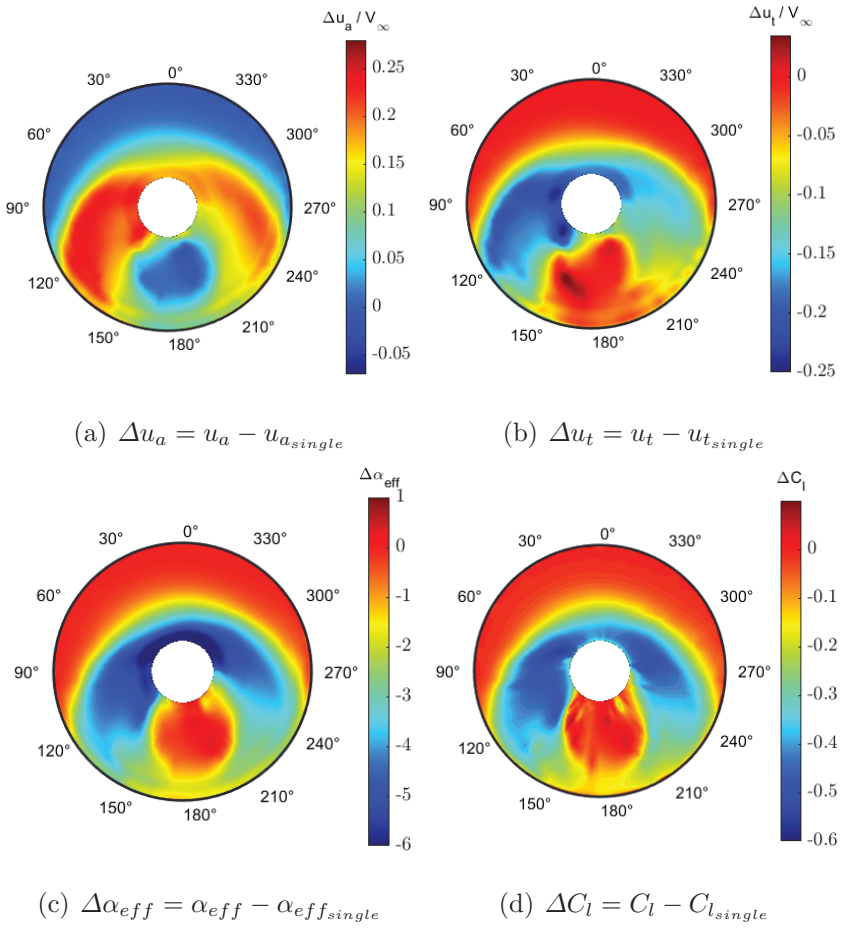

(a) $\Delta u_a = u_a - u_{a_{single}}$ (b) $\Delta u_t = u_t - u_{t_{single}}$

(c) $\Delta \alpha_{eff} = \alpha_{eff} - \alpha_{eff_{single}}$ (d) $\Delta C_l = C_l - C_{l_{single}}$

Figure 12: Variations of the axial velocity, tangential velocity, effective angle of attack and sectional lift coefficient computed by DUST simulations at $J = 0.8$ on the rear propeller blade in tandem configurations with respect to the single rotor configuration for the last rotor revolution, $L_x = 5$R, $L_y = 0.5$R, $Re_D = 1.96 \cdot 10^6$, $M_t = 0.325$.

Similar considerations can be made from the analysis of simulations results obtained for the tandem propellers configuration with $L_y = 1R$, where similar effects provided by front propeller slipstream on rear propeller blade velocity components are observed over a smaller region of blade azimuthal phase angle, due to the lower degree of overlapping area between propellers disks. Consequently, sectional lift coefficient losses are experienced only by airfoils over a small portion of rear propeller blade azimuthal phase angle

(see Figs. 13(c) and 13(d)), thus physically reflecting the lower detrimental effects on the average propeller aerodynamic performance observed for this configuration with respect to the test cases characterised by a higher degree of overlapping between propellers disks.

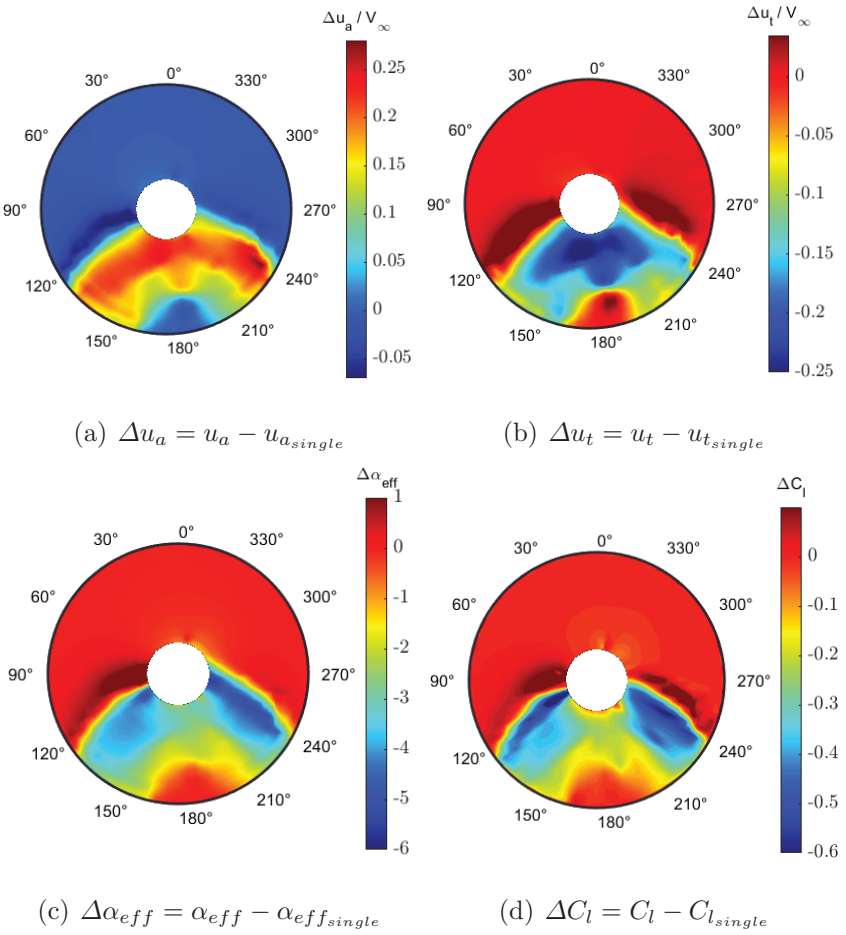

(a) $\Delta u_a = u_a - u_{a_{single}}$ (b) $\Delta u_t = u_t - u_{t_{single}}$

(c) $\Delta \alpha_{eff} = \alpha_{eff} - \alpha_{eff_{single}}$ (d) $\Delta C_l = C_l - C_{l_{single}}$

Figure 13: Variations of the axial velocity, tangential velocity, effective angle of attack and sectional lift coefficient computed by DUST simulations at $J = 0.8$ on the rear propeller blade in tandem configurations with respect to the single rotor configuration for the last rotor revolution, $L_x = 5\text{R}$, $L_y = 1\text{R}$, $Re_D = 1.96 \cdot 10^6$, $M_t = 0.325$.

In addition to the average propeller performance analysis, another aspect to be studied, particularly interesting for acoustic issues, is the evaluation

of the effects of aerodynamic interaction on the dynamic behaviour of aerodynamic loads acting on rear propeller in tandem configurations. With this aim, the time histories of thrust coefficients computed by DUST simulations on rear propeller in different tandem configurations for $J = 0.8$ are compared in Fig. 14.

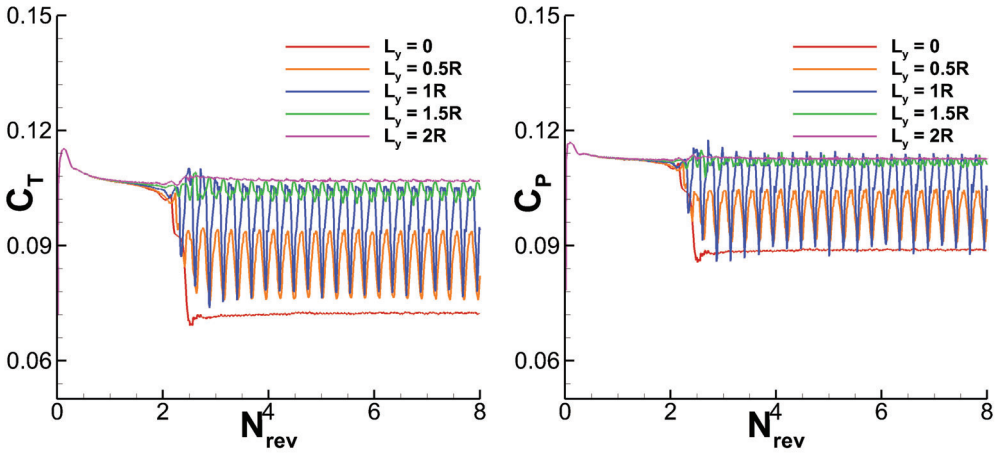

(a) (b)

Figure 14: Comparison of the time histories of the thrust coefficients computed by DUST simulations for the rear propeller in tandem configurations at $J = 0.8$, $L_x = 5$R, $Re_D = 1.96 \cdot 10^6$, $M_t = 0.325$.

The C_T curve computed for tandem configuration with propellers disks completely overlapped, i.e. $L_y = 0$, shows negligible thrust fluctuations experienced by rear propeller due to front propeller slipstream interaction. Indeed, the complete superposition of front propeller slipstream with rear propeller disk provide an axial-symmetrical distribution of the aerodynamic loads acting on rear propeller blade with respect to azimuthal phase angle, as highlighted by the computed blade sectional lift shown in Fig. 11(d). This explains the negligible amount of loads fluctuation characterising this co-axial tandem configuration. On the other hand, when the superposition

area between propellers disks decreases, the rear propeller thrust time history shows a periodic behaviour starting after 3 rotor revolutions that reflects the beginning of aerodynamic interactional effects due to front propeller wake ingestion. In particular, the peak-to-peak value of thrust periodic oscillations becomes higher decreasing the degree of overlapping between propellers disks up to $L_y = 1\text{R}$, where rear propeller experiences the thrust fluctuations with highest amplitude. The larger thrust fluctuations observed for this tandem configurations are justified by the high non-symmetrical distribution of rear propeller blade airfoils sectional lift along a rotor revolution that is provided by the partial ingestion of the front propeller slipstream (see Fig. 13(d)). Further increasing the lateral distance between tandem propellers, i.e. $L_y = 1.5\text{R}$, the thrust fluctuation amplitude decreases and becomes almost negligible when the degree of overlapping between propellers disks becomes null, i.e. $L_y = 2\text{R}$.

The outcomes of numerical simulations concerning the dynamic behaviour of aerodynamic loads acting on rear propeller blades for the different analysed configurations is confirmed by experiments, as highlighted by Fig. 15 showing the spectra of thrust signals measured on single and rear propeller model for the test cases with advance ratio $J = 0.8$. As during the wind tunnel tests the blade azimuth phase angle of the two three-bladed propellers was not synchronised, the aerodynamic interactional effects on rear propeller in tandem is highlighted by the 6/rev peaks in the thrust signals spectra comparison. In particular, analogously to what observed from numerical results analysis, the amplitude of the 6/rev peaks becomes higher by decreasing the degree of overlapping between propeller disks and reaches the maximum value for $L_y = 1\text{R}$, thus confirming that the highest level of thrust fluctuation is obtained for this configuration.

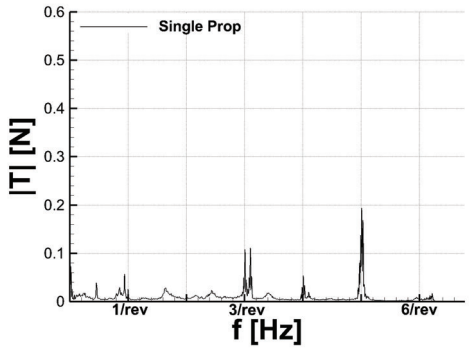

(a) Single Prop

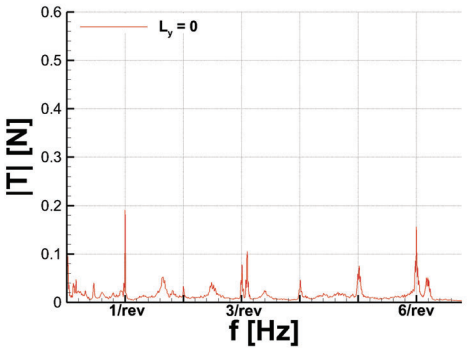

(b) $L_y = 0$

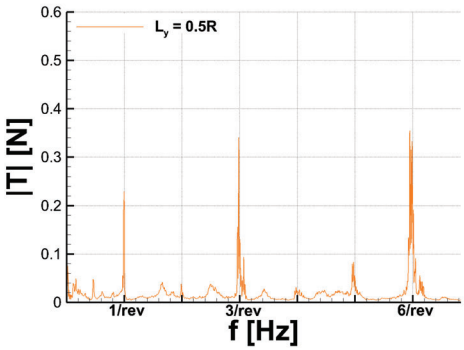

(c) $L_y = 0.5\text{R}$

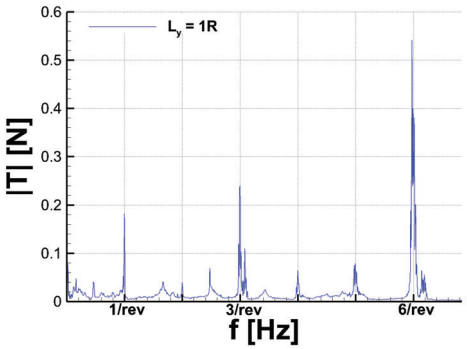

(d) $L_y = 1\text{R}$

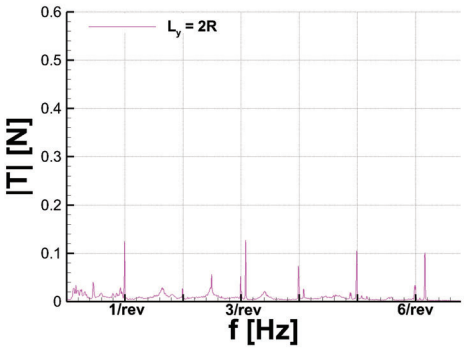

(e) $L_y = 2\text{R}$

Figure 15: Comparison of the measured rear propeller thrust spectra at $J = 0.8$, $L_x = 5\text{R}$, $Re_D = 1.96 \cdot 10^6$, $M_t = 0.325$.

Consequently, the propeller performance analysis based on experimen-

tal and numerical results provides different insights suitable for the design of novel aircraft architectures characterised by overlapping propellers in tandem. Indeed, aerodynamics interaction between propellers provides the highest detrimental effects in terms of rear propeller performance losses when the propellers disks are completely overlapped, i.e. co-axial configuration. On the other hand, a partial overlap between propeller disks improves the rear propeller average aerodynamic performance but is responsible for a quite higher level of aerodynamic loads fluctuations, representing a drawback for aeroacoustic issues, particularly important in the design of vehicles operating in urban areas.

4.2. Flow field analysis

A detailed insight about flow physics involved in the aerodynamic interaction between the investigated tandem propellers configurations is provided by the analysis of flow fields evaluated by PIV surveys and numerical simulations at $J = 0.8$ for three lateral distances between propellers, i.e. $L_y = 0$, $L_y = 0.5$R and $L_y = 1$R. In particular, flow fields analysis is provided in the following by the comparison of the contours of the average freestream (u) and out-of-plane (w) velocity components. In order to help the comparison between experimental and simulations results, the boundaries of PIV fields of view are depicted with black dashed lines on numerical flow fields. Moreover, a quantitative analysis is provided by the comparison of u and w velocity profiles extracted along vertical direction (Y) at three different longitudinal positions, i.e. $X/R = 0.25$, $X/R = 0.5$ and X/R =1. In particular, PIV results are here ensemble-averaged over the free-run surveys data, while numerical flow fields are here averaged over time steps of last rotor revolution.

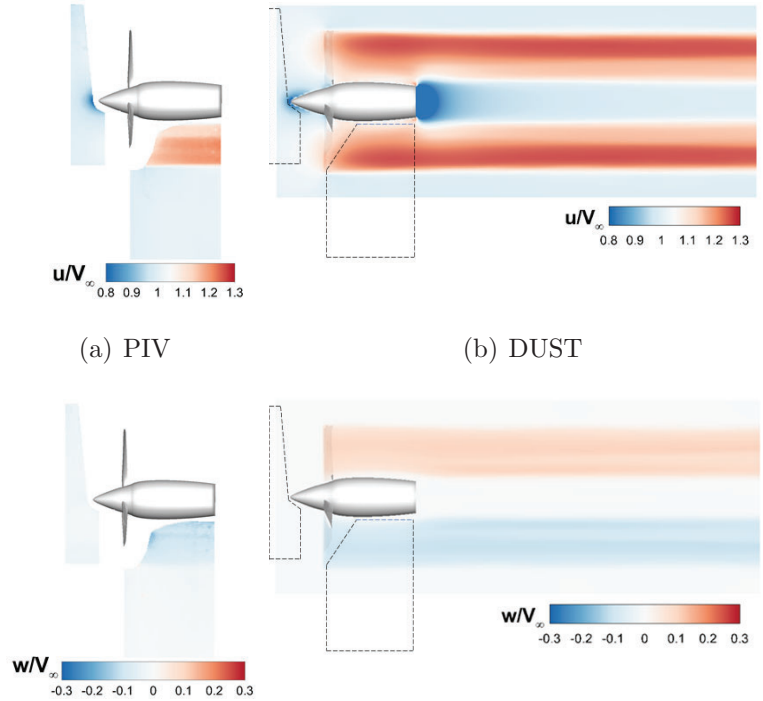

(a) PIV (b) DUST

(c) PIV (d) DUST

Figure 16: Comparison of the averaged freestream and out-of-plane velocity components for single propeller configurations at $J = 0.8$, $Re_D = 1.96{\cdot}10^6$, $M_t = 0.325$. The boundaries of PIV fields of view are depicted with black dashed lines on numerical flow fields

Averaged flow fields analysis for single propeller configuration highlights the suitability of numerical model to reproduce aerodynamics features of the present propeller. Indeed, a quite good agreement between PIV and simulation results was found for the global flow behaviour in the wake of the single propeller for both freestream (u) and out-of-plane (w) velocity components (see Fig. 16). Moreover, the larger field of view provided by numerical results enabled to observe a small contraction of propeller slipstream core with respect to axial coordinate X. In particular, in order to provide a quantitative indication of slipstream contraction, the velocity peak-to-peak distance evaluated on the vertical freestream velocity component profile at $X/R = 5$

is 4.5%R lower with respect to the one evaluated in correspondence of the propeller disk position ($X/R = 0$).

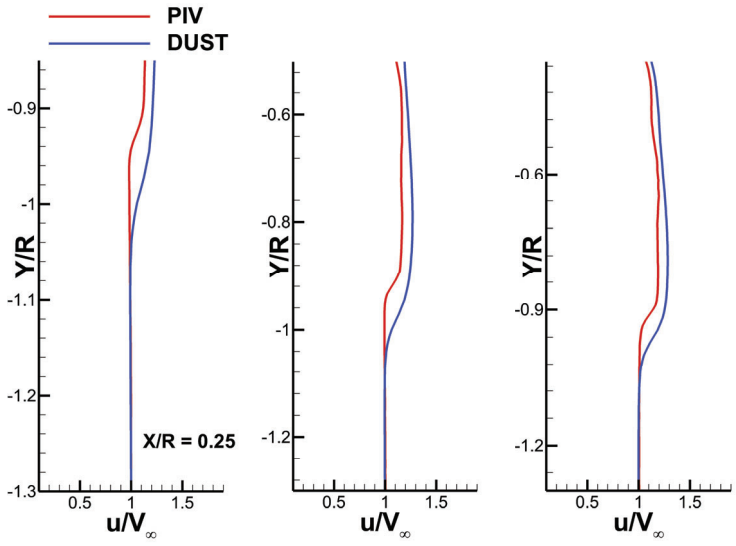

(a) $X/R = 0.25$ (b) $X/R = 0.5$ (c) $X/R = 1$

Figure 17: Comparison of the averaged freestream velocity component profiles for single propeller configurations at $J = 0.8$, $Re_D = 1.96 \cdot 10^6$, $M_t = 0.325$.

The quantitative u velocity profiles comparison (see Fig. 17) indicates that simulations exposed a slightly wider accelerated flow region imposed by propeller to slipstream with respect to experiments, characterised also by an increase of u values that are below 8% of freestream velocity (V_∞). Moreover, a quite coherent behaviour of the out-of-plane w velocity profiles is observed between PIV and DUST simulations results, with a quite good agreement of the quantitative values of w velocity along slipstream flow region (see Fig. 18).

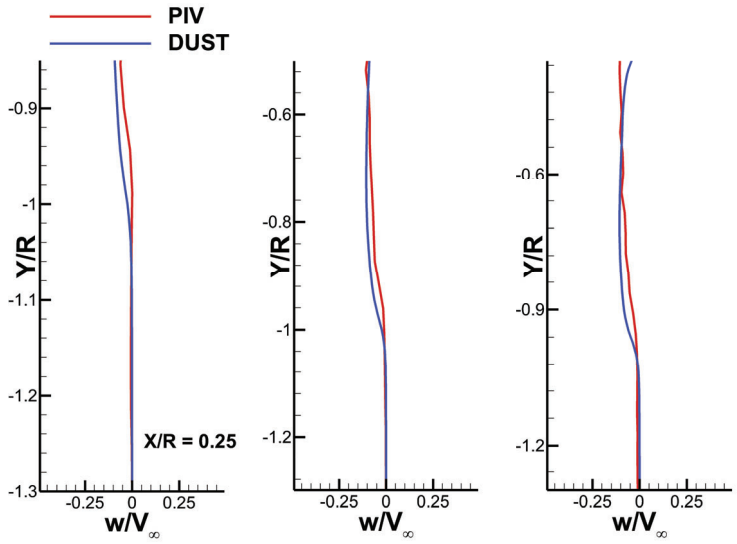

(a) $X/R = 0.25$ (b) $X/R = 0.5$ (c) $X/R = 1$

Figure 18: Comparison of the averaged out-of-plane velocity component profiles for single propeller configurations at $J = 0.8$, $Re_D = 1.96 \cdot 10^6$, $M_t = 0.325$.

For the co-axial tandem propeller configuration, i.e. $L_y = 0$, PIV results at rear propeller inflow region (see Fig. 19(a)) clearly highlight that front propeller slipstream produces an acceleration of rear propeller outer wake region with respect to single propeller configuration. Moreover, the ingestion of the co-rotating front propeller slipstream provides a rather increase of swirl velocity component in the wake of the co-axial rear propeller (see Fig. 19(c)). Both the accelerated flow and the swirled flow regions passing through the outer areas of tandem propellers disks are well captured by numerical simulations, showing for co-axial configuration a quite symmetrical flow field for both the investigated velocity components (see Figs. 19(b) and 19(d)). Nevertheless, the quantitative comparison between freestream velocity component profiles shows differences between PIV and DUST results along rear propeller slipstream flow region below 15% of freestream velocity (V_∞), see Fig. 20. On the other hand, a higher agreement is found for out-of-plane

velocity profiles (see Fig. 21).

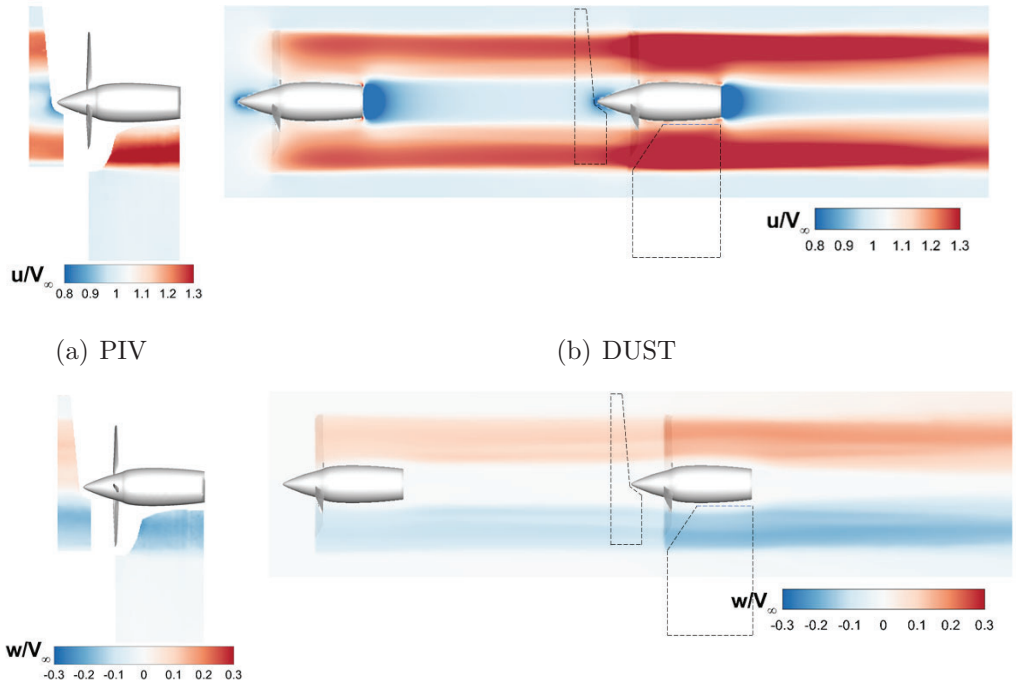

(a) PIV (b) DUST

(c) PIV (d) DUST

Figure 19: Comparison of the averaged freestream out-of-plane velocity components for the tandem propellers configuration with $L_x = 5$R and $L_y = 0$ at $J = 0.8$, $Re_D = 1.96 \cdot 10^6$, $M_t = 0.325$. The boundaries of PIV fields of view are depicted with black dashed lines on numerical flow fields.

The wider field of view provided by numerical simulations highlights two additional information. First of all, a higher contraction of rear propeller slipstream can be observed while comparing rear propeller wake with single propeller one. In particular, a 2%R reduction of the velocity peak-to-peak distance evaluated over the vertical freestream velocity component profile extracted at $X/R = 5$ is found with respect to single propeller configuration. In second place, comparing the front propeller wake with single propeller one, a quite similar behaviour can be observed, thus reflecting that the front

propeller is negligible affected by rear propeller interaction.

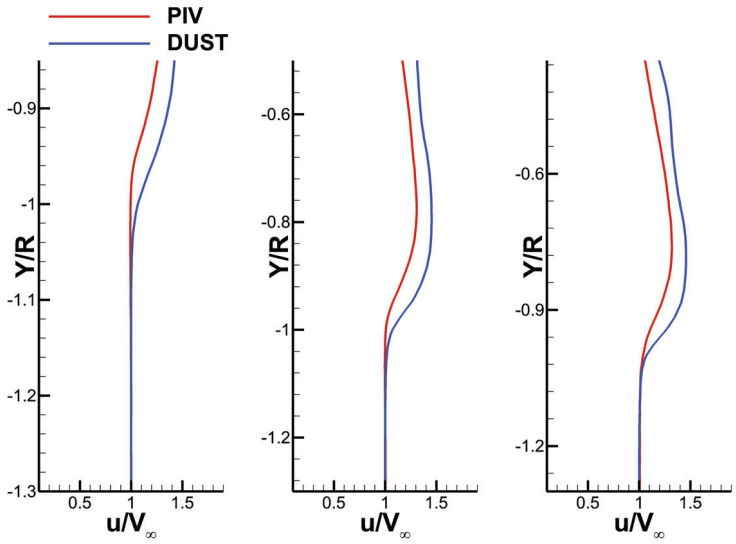

(a) $X/R = 0.25$ (b) $X/R = 0.5$ (c) $X/R = 1$

Figure 20: Comparison of the averaged freestream velocity component profiles for the tandem propellers configuration with $L_x = 5$R and $L_y = 0$ at $J = 0.8$.

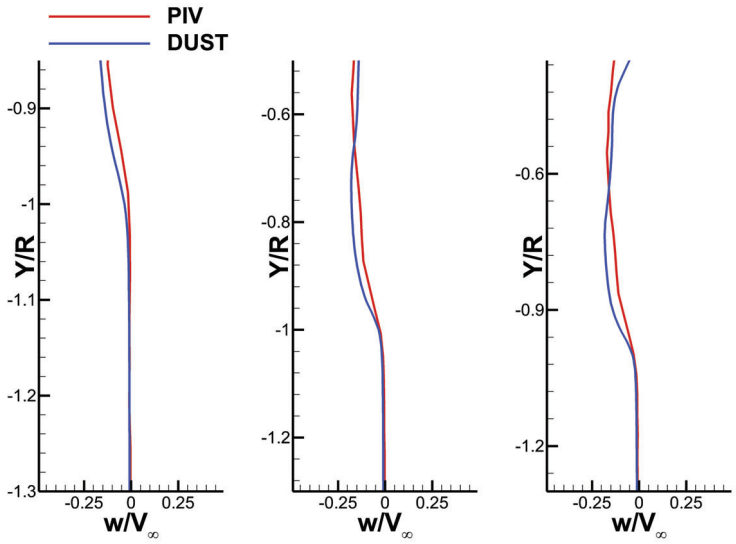

(a) $X/R = 0.25$ (b) $X/R = 0.5$ (c) $X/R = 1$

Figure 21: Comparison of the averaged out-of-plane velocity component profiles for the tandem propellers configuration with $L_x = 5$R and $L_y = 0$ at $J = 0.8$.

Increasing the separation distance between propellers to $L_y = 0.5$R, an asymmetrical behavior of rear propeller inflow is observed from PIV measurements (see Figs. 22(a) and 22(c)). In particular, the upper region of front propeller slipstream is dragged upward by the rear propeller nacelle curvature. Consequently, this provides a streamlined accelerated flow region occurring over the nacelle area of rear propeller wake, as can be observed from numerical simulations results shown in Fig. 22(b). The very same region is also characterised by a slightly increased positive out-of plane velocity (see Fig.22(c)). Moreover, PIV results show a larger flow deceleration in front the nacelle with respect to simulations related to the impinging of the upper region of front propeller slipstream on propeller spinner.

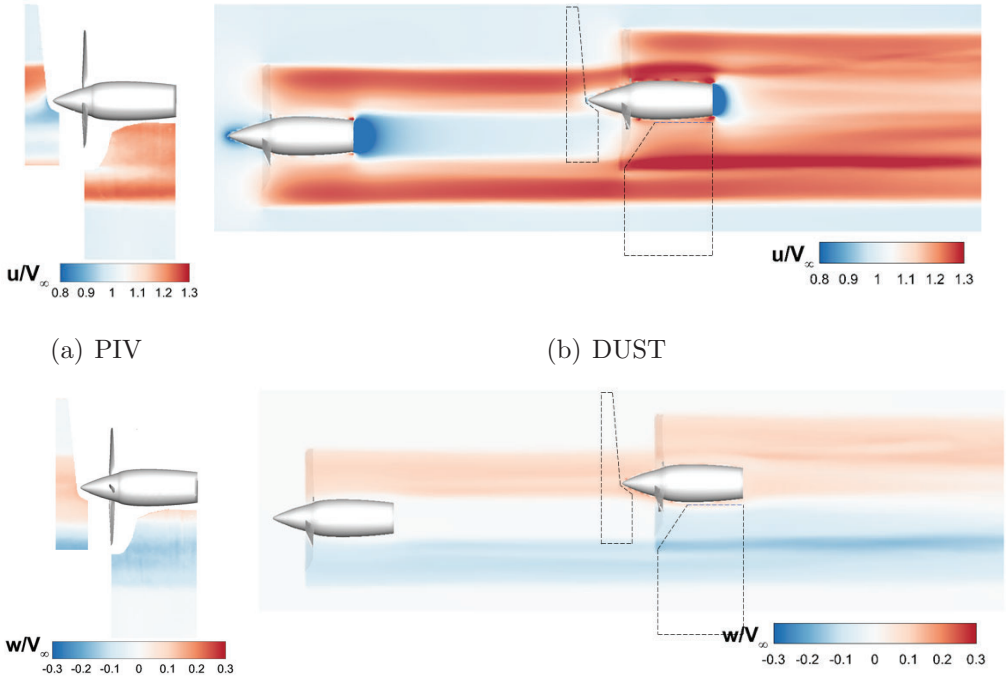

(a) PIV (b) DUST

(c) PIV (d) DUST

Figure 22: Comparison of the averaged freestream out-of-plane velocity components for the tandem propellers configuration with $L_x = 5\text{R}$ and $L_y = 0.5\text{R}$ at $J = 0.8$, $Re_D = 1.96 \cdot 10^6$, $M_t = 0.325$. The boundaries of PIV fields of view are depicted with black dashed lines on numerical flow fields.

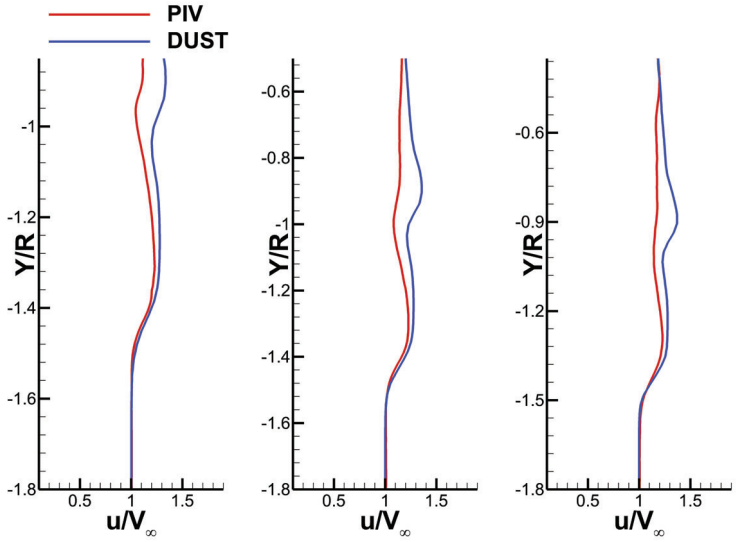

(a) $X/R = 0.25$ (b) $X/R = 0.5$ (c) $X/R = 1$

Figure 23: Comparison of the averaged freestream velocity component profiles for the tandem propellers configuration with $L_x = 5\text{R}$ and $L_y = 0.5\text{R}$ at $J = 0.8$.

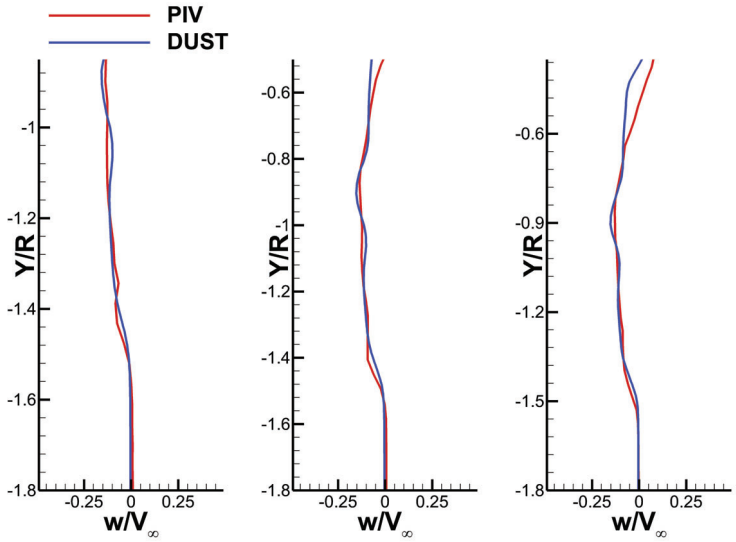

(a) $X/R = 0.25$ (b) $X/R = 0.5$ (c) $X/R = 1$

Figure 24: Comparison of the averaged out-of-plane velocity component profiles for the tandem propellers configuration with $L_x = 5\text{R}$ and $L_y = 0.5\text{R}$ at $J = 0.8$.

Moreover, the lower region of front propeller slipstream interacts with the lower portion of rear propeller wake, as clearly visible from PIV measurements performed in the wake area. This interaction provides a non-uniform accelerated flow region past the rear propeller disk. The resulting complex interactional flow field in this region presents some discrepancies between experiments and simulations. Indeed, the rear propeller slipstream acceleration at about Y/R = -0.9 is quite lower for PIV results with respect to simulations (see the coloured contours of free-stream velocity components in Figs. 22(a) and 22(b)). This feature is quantitatively highlighted by u velocity component profiles comparison, particularly at $X/R = 0.25$, where a difference in the order of 20% of free-stream velocity (V_∞) can be observed between PIV and DUST results above Y/R = -0.9. Moreover, the lower flow region past the rear propeller disk is also characterised by an increased negative swirl that expands as long as wake progresses further from nacelle trailing edge (see numerical results in Figs. 22(d)) The quantitative comparison of the out-of-plane velocity component outlines an overall agreement between the averaged profiles behaviour exposed by PIV and DUST, even if a certain discrepancy of the local concavity of the w velocity profiles can be observed related to the complexity of the interactional flow field in this region.

For the tandem propellers configuration with lateral separation distance L_y = 1R, the inflow PIV measurements show that the upper half of rear propeller disk is not influenced by front propeller slipstream, thus experiencing almost uniform free-stream and almost null out-of plane velocity conditions.

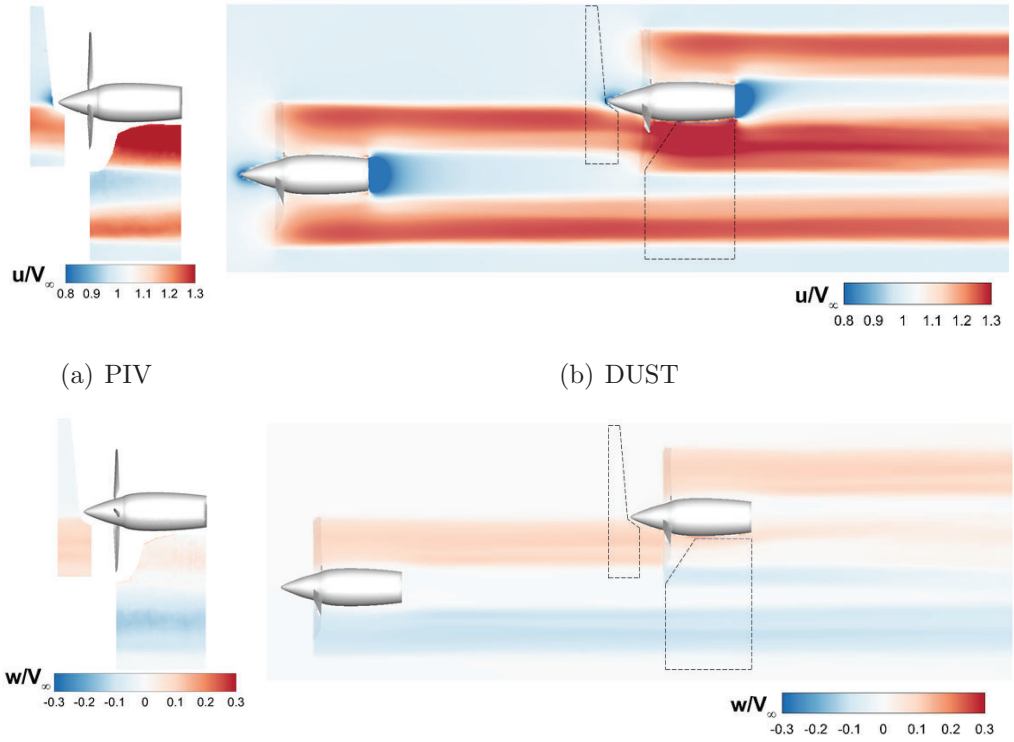

(a) PIV (b) DUST

(c) PIV (d) DUST

Figure 25: Comparison of the averaged freestream out-of-plane velocity components for the tandem propellers configuration with $L_x = 5\text{R}$ and $L_y = 1\text{R}$ at $J = 0.8$, $Re_D = 1.96 \cdot 10^6$, $M_t = 0.325$. The boundaries of PIV fields of view are depicted with black dashed lines on numerical flow fields.

On the other hand, the lower half portion of the rear propeller disk is fully invested by front propeller upper slipstream, leading to an accelerated flow region past this disk area (see Fig. 25(a)). Moreover, as the lower portion of rear propeller disk, naturally characterised by negative swirl velocity, is invested by the upper front propeller slipstream characterised by positive swirl velocity, the resulting out-of plane velocity is quite reduced in the flow region past this disk area with respect to the previous configurations (see Fig. 25(c)). These features are well captured by numerical simulations. In particular, numerical results capture the significant flow acceleration in the

lower portion of rear propeller wake and a quite good quantitative agreement with PIV results can be observed from u velocity profiles comparison shown in Fig. 26. Moreover, flow field colour maps and velocity profiles highlight the high degree of flow asymmetry occurring for this configuration below the rear propeller, as this wake portion is dragged downward immediately after propeller disk (see Figs. 25(b) and 26). The quite complex behaviour of rear propeller slipstream lower region occurring due to the interactional mechanisms with front propeller slipstream is also highlighted by the out-of-plane velocity representation of numerical results showing the coexistence of two flow regions with opposite swirl velocity component (see Fig. 25(d)). In particular, simulations results show a negative component of w above Y/R = -0.9, while PIV results exposed a negligible swirl velocity contribution n this area (see Fig. 27).

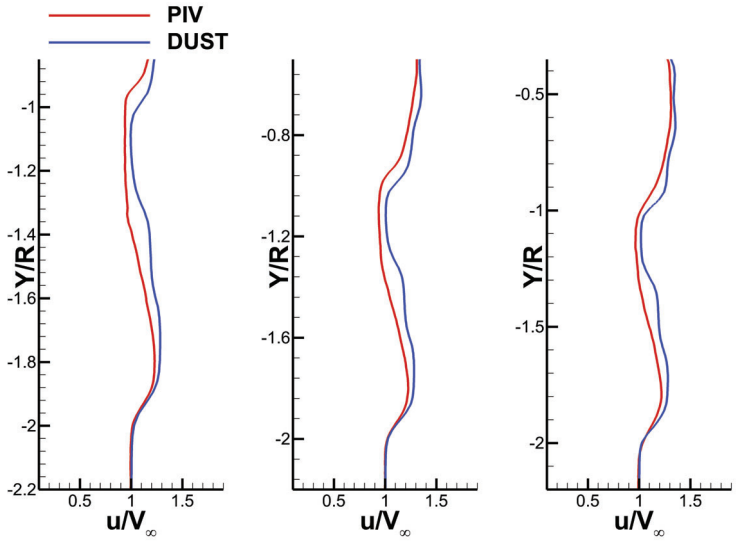

(a) $X/R = 0.25$ (b) $X/R = 0.5$ (c) $X/R = 1$

Figure 26: Comparison of the averaged freestream velocity component profiles for the tandem propellers configuration with L_x = 5R and L_y = 1R at J = 0.8.

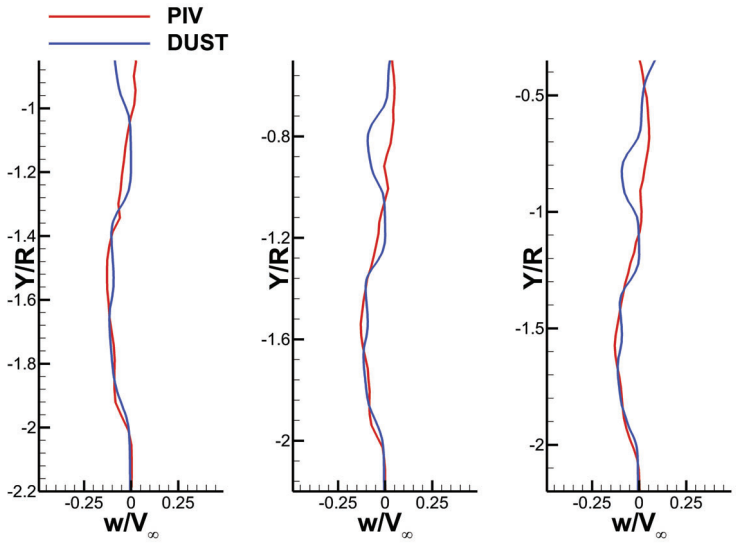

(a) $X/R = 0.25$ (b) $X/R = 0.5$ (c) $X/R = 1$

Figure 27: Comparison of the averaged out-of-plane velocity component profiles for the tandem propellers configuration with $L_x = 5\text{R}$ and $L_y = 1\text{R}$ at $J = 0.8$.

Further details about the vortex-vortex interactions occurring for the investigated tandem propellers configurations is provided by the analysis of instantaneous flow fields evaluated by phase-locked PIV surveys and numerical simulations. The spatial resolution of the present PIV measurement is considered sufficient to characterise the propellers tip vortex characteristics above core radius, as shown by results of a previous work by one of the authors employing the same propeller models and instrumentation set up [41]. Figure 28 shows the comparison of the instantaneous out-of-plane vorticity component evaluated by phase-locked PIV measurements and numerical simulations at $\psi = 170°$. In particular, the comparison includes both the single and the tandem propellers configurations characterised by lateral distances $L_y = 0$, $L_y = 0.5\text{R}$ and $L_y = 1\text{R}$ at $J = 0.8$. Moreover, in order to obtain a three-dimensional representation of the vortices behaviour, numerical re-

sults show an iso-surface of Q-criterion superimposed to vorticity contours. Instantaneous flow fields comparison should consider that experimental data were obtained by phase-averaging PIV measurements data triggered by rear propeller blade azimuthal angle position, i.e. the front propeller operated in free-run condition, while numerical results were obtained by simulations of the two tandem propellers having synchronised blade azimuthal phase. The choice to present phase-averaged PIV data with respect to rear propeller blade azimuthal angle is dictated by the will to focus the present analysis on a more detailed investigation of the front propeller slipstream interactional effects on the flow field past the rear propeller.

The out-of-plane vorticity and Q-criterion iso-surface representation of the instantaneous flow field evaluated for single propeller configuration clearly show the periodic release of the blades tip and root vortices associated with the footprint of the shear layers produced by the rotating blades. In particular, for the single propeller the comparison between phase-averaged PIV data and numerical simulation results highlights a quite good agreement in terms of vortices core position and intensity inside propeller wake (see Figs. 28(a) and 28(b)).

For co-axial tandem propellers configuration, PIV results clearly show in the inflow measurement area the traces of the blades tip vortices issued by the front propeller rotating in free-run condition and delimiting the slipstream investing the rear propeller disk. Consequently, due to an interaction with front propeller slipstream, the rear propeller tip vortex captured in the PIV wake measurement area presents a lower level of vorticity with respect to single propeller configuration (see Figs. 28(a) and 28(c)). In particular, due to this interaction only a shaded trace of the second tip vortex can be appreciated at the right edge of PIV field of view in the wake of rear

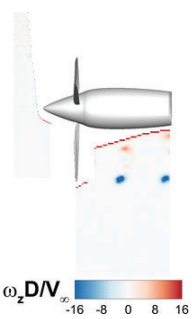

(a) PIV - Single Prop

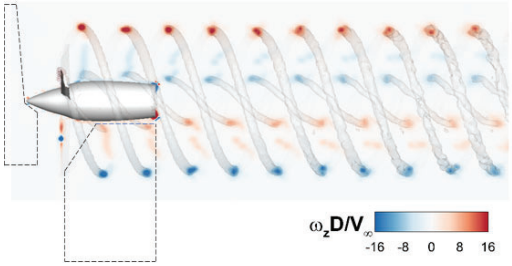

(b) DUST - Single Prop

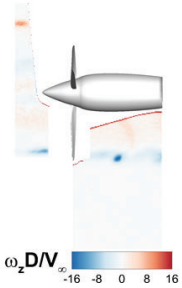

(c) PIV - $L_y = 0$

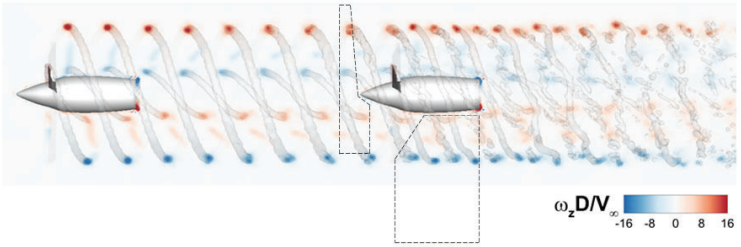

(d) DUST -$L_y = 0$

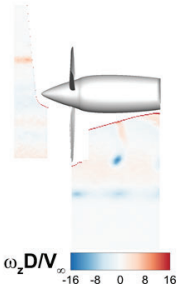

(e) PIV - $L_y = 0.5$R

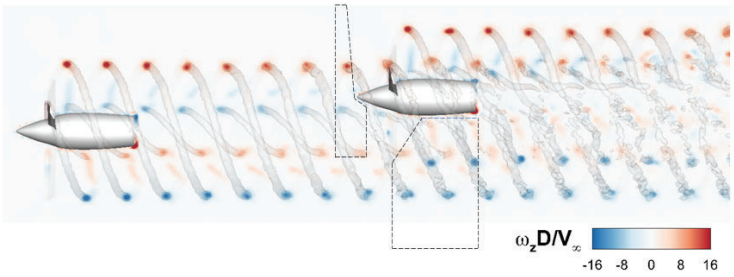

(f) DUST - $L_y = 0.5$R

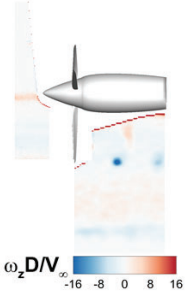

(g) PIV - $L_y = 1$R

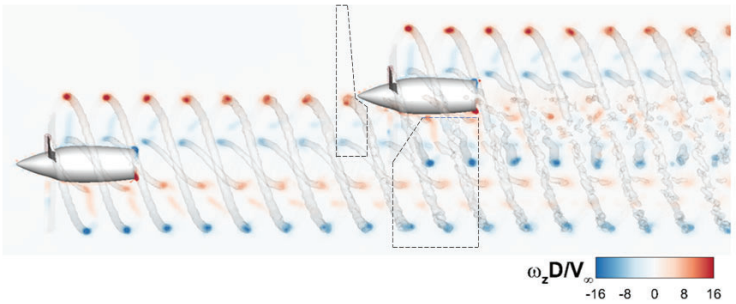

(h) DUST - $L_y = 1$R

Figure 28: Comparison of the instantaneous out-of-plane vorticity component and iso-surface of Q-criterion, $Q_{crit} = 1e5$, for the single and tandem propellers configurations with $L_x = 5$R at $J = 0.8$, $\psi = 170°$, $Re_D = 1.96 \cdot 10^6$, $M_t = 0.325$. The boundaries of PIV fields of view are depicted with black dashed lines on numerical flow fields.

propeller. Numerical results for co-axial propellers configuration clearly show a double array of tip vortices in the wake of the rear one as a results of the rotation of two propellers (see 28(d)). In particular, Q-criterion iso-surface representation highlights that, due to front propeller slipstream interaction, the helical structure provided by rear propeller blades tip vortices looses coherence quite earlier with respect to front propeller one. Consequently, a higher degree of dissipation can be observed for rear propeller blade tip vortices, as shown by the vorticity level evaluated past the rear propeller disk. Due to the co-axial configuration of tandem propellers, similar considerations can be done analysing the behaviour of the blades root vortices past the rear propeller disk.

For tandem propellers configuration with $L_y = 0.5$R, PIV results indicate that rear propeller blades tip vortices immersed in the accelerated region of front propeller slipstream experience a slight higher dissipation with respect to co-axial configuration (see Fig. 28(e)). Indeed, as confirmed by numerical results, this effect is provided by the interaction with the blades root vortices issued by the front propeller. This interaction makes the second tip vortex captured by PIV scarcely visible, as shown by the shaded blue trace that can be appreciated at the right edge of rear propeller wake PIV field of view. Moreover, numerical results highlight that the upper array of tip vortices issued by the front propeller blades is dragged upward due to the cambered shape of the spinner-nacelle assembly, thus providing an interaction with the root vortices array issued by rear propeller blades (see Fig. 28(f)). Generally speaking, the helical structure associated with rear propeller blades tip vortices looses coherence only in the area affected by front propeller slipstream interaction, as shown by Q-criterion iso-surface representation.

For tandem propellers configuration with $L_y = 1$R, PIV results show that

tip vortices released by rear propeller blades present a lower degree of dissipation with respect to the previous analysed tandem propellers configurations (see Fig. 28(g)). This effect is due to the fact that, in this case, the lower array of rear propeller blades tip vortices is positioned between the double array of root vortices released by front propeller blades, as clearly shown by numerical results (see Fig. 28(h)). Moreover, numerical results shows enhanced information about wake interaction. In particular, once blades tip vortices delimiting the higher edge of the front propeller slipstream impinge on the rear propeller spinner, they dissipate and their trace become almost negligible downstream the rear propeller disk. A mutual vortex interaction can be also observed between the upper array of vortices issues by front propeller blades root and the lower array of vortices issues by rear propeller blades tips. Generally, for this tandem configuration, Q-criterion iso-surface representation shows that only the lower half of the helical structure associated with rear propeller blades tip vortices looses coherence due to front propeller slipstream interaction.

5. Conclusions

A systematic series of wind tunnel tests was performed to investigate the effects of aerodynamic interactions between two overlapping propellers reproducing typical airplane mode flight conditions of eVTOLs. Loads and flow field measurements enabled to achieve details on interactional effects on propellers performance and on the complex flow physics involved in such configurations. Moreover, numerical simulations were firstly validated against experimental results and then used to enhance the physical comprehension of performance measurements as well as to achieve a more detailed and a wider overview of the interacting wakes phenomena. The main achievements

of the present work are summarised in the following.

Loads measurements enabled to quantify detrimental effects on rear propeller aerodynamic performance for configurations with different degree of overlapping between tandem propellers disks. Loads analysis highlighted the highest performance losses in terms of rear propeller thrust for co-axial configuration, while the highest fluctuations of loads on rear propeller blades were found when propeller disks are partially overlapped, i.e. with lateral distance between rotation axis equal to one propeller radius. Consequently, aerodynamic performance measurements indicated that a co-axial propellers configuration in airplane mode is responsible for a severe decrease of rear propeller thrust, in the order of 30% for the present test case, while spectral analysis of measured thrust signals indicated that vehicle configurations considering partial overlapped configurations between tandem propellers have to consider more severe issues in terms of acoustic impact. Numerical simulations results clearly explained the aerodynamic mechanisms responsible for the larger performance losses observed on rear propeller when increasing the degree of overlapping between tandem propellers disks. Indeed, simulations results highlighted that rear propeller blades sections invested by front propeller slipstream experience a modification of the local inflow providing a local decrease of angle of attack with respect to single propeller configuration. Moreover, the analysis of rear propeller loads time histories computed by simulations confirmed that the highest interactional effects are found for tandem propellers with separation distance equal to one radius, as this configuration shows the highest amplitude of rear propeller loads fluctuations, analogously to what exposed by spectral analysis of measured thrust signals.

Stereo PIV surveys enabled to investigate the interacting flow fields between overlapping tandem propellers and represented a novel contribution

with respect to literature concerning the study of such propellers configurations for airplane mode flight conditions. Moreover, PIV results enabled to validate the outcomes of mid-fidelity aerodynamic simulations for such a demanding test case. In particular, the analysis of experimental and numerical flow fields indicates how the front propeller slipstream influences the rear propeller wake when separation distance between propellers is increased and highlighted in details the complex interactions occurring between vortices arrays issued by both blades roots and tips of the tandem propellers.

Generally, the experimental and numerical database obtained over a simplified but informative test case for eVTOL vehicles provided interesting guidelines for the optimal design of such innovative vehicle configurations. Moreover, the present experimental data are suitable for the validation of CFD tools with different fidelity to be used for aerodynamic studies of complete eVTOL aircraft.

Acknowledgements

This research has received no funding.

References

[1] N. Polaczyk, E. Trombino, P. Wei, M. Mitici, A review of current technology and research in urban on-demand air mobility applications, in: Proceedings of the Vertical Flight Society's 6th Annual Electric VTOL Symposium, Mesa, AZ, USA, 2019.

[2] W. Johnson, C. Silva, E. Solis, Concept vehicles for vtol air taxi operations, in: Proceedings of the AHS Technical Conference on Aeromechanics Design for Transformative Vertical Flight, AHS International, San Francisco, CA, USA, 2018.

[3] C. Silva, W. Johnson, E. Solis, M. D. Patterson, K. R. Antcliff, Vtol urban air mobility concept vehicles for technology development, in: Proceedings of the AIAA Aviation Technology, Integration, and Operations Conference, AIAA, Atlanta, GA, USA, 2018.

[4] G. Droandi, M. Syal, G. Bower, Tiltwing multi-rotor aerodynamic modeling in hover, transition and cruise flight conditions, in: Proceedings of the 74th Annual Forum, AHS International, Phoenix, 2018.

[5] F. Harris, Technical note: Twin rotor hover performance, Journal of the American Helicopter Society 44 (1) (1999) 34–37.

[6] M. Ramasamy, Hover performance measurements toward understanding aerodynamic interference in coaxial, tandem, and tilt rotors, Journal of the American Helicopter Society 60 (3) (2015) 1–17.

[7] H. H. Heyson, Preliminary results from flow-field measurements around single and tandem rotors in the langley full-scale tunnel, Tech. rep., NACA TN 3242 (1954).

[8] R. Boisard, J. W. Lim, Aerodynamic analysis of rotor/propeller wakes interactions on high speed compound helicopter, in: Proceedings of the 47th European Rotorcraft Forum, Virtual Event, 2021.

[9] D. Shukla, N. Hiremath, K. NM, Low reynolds number aerodynamics study on coaxial and quad-rotor, in: Proceedings of the 53th AIAA Aviation Forum, Atlanta, GA, USA, 2018.

[10] M. Brazinskas, S. Prior, J. Scanlan, An empirical study of overlapping rotor interference for a small unmanned aircraft propulsion system, aerospace 3 (32) (2016).

[11] S. Yoon, H. Lee, T. Pulliam, Computational analysis of multi-rotor flows, in: Proceedings of the 54th AIAA Aerospace Sciences Meeting, San Diego, CA, USA, 2016.

[12] P. Ventura Diaz, S. Yoon, High-fidelity computational aerodynamics of multi-rotor unmanned aerial vehicles, in: Proceedings of the 56th AIAA Aerospace Sciences Meeting, Kissimmee, FL, USA, 2018.

[13] W. Zhou, Z. Ning, H. Li, H. Hu, An experimental investigation on rotor-to-rotor interactions of small uav propellers, in: Proceedings of the 35th AIAA Applied Aerodynamics Conference, Denver, USA, 2017.

[14] D. Shukla, N. Komerath, Multirotor drone aerodynamic interaction investigation, Drones 2 (4) (2018) 1–13.

[15] R. de Vries, N. van Arnhem, T. Sinnige, R. Vos, L. L. Veldhuis, Aerodynamic interaction between propellers of a distributed-propulsion system in forward flight, Aerospace Science and Technology 118 (2021) 107009. doi:https://doi.org/10.1016/j.ast.2021.107009.
URL https://www.sciencedirect.com/science/article/pii/S1270963821005198

[16] J. Yin, S. Ahmed, Helicopter main-rotor/tail-rotor interaction, Journal of the American Helicopter Society 4 (2000) 293–302.

[17] M. Tugnoli, D. Montagnani, M. Syal, G. Droandi, A. Zanotti, Mid-fidelity approach to aerodynamic simulations of unconventional vtol aircraft configurations, Aerospace Science and Technology 115 (2021) 106804. doi:https://doi.org/10.1016/j.ast.2021.106804.
URL https://www.sciencedirect.com/science/article/pii/S127096382100314X

[18] M. Wentrup, J. Yin, P. Kunze, T. Streit, J. Wendisch, T. Schwarz, J. Pinacho, K. K, R. Fukari, An overview of dlr compound rotorcraft

aerodynamics and aeroacoustics activities within the cleansky2 nacor project, in: Proceedings of 74th AHS Annual Forum & Technology Display, Phoenix, AZ, USA, 2018.

[19] J. Tan, T. Zhou, J. Sun, G. Barakos, Numerical investigation of the aerodynamic interaction between a tiltrotor and a tandem rotor during shipboard operations, Aerospace Science and Technology 87 (2019) 62–72.

[20] G.-H. Cottet, P. D. Koumoutsakos, D. Petros, et al., Vortex methods: theory and practice, Cambridge University Press, 2000.

[21] G. S. Winckelmans, Topics in vortex methods for the computation of three-and two-dimensional incompressible unsteady flows, Ph.D. thesis, California Institute of Technology (1989).

[22] E. Alvarez, A. Ning, Modeling multirotor aerodynamic interactions through the vortex particle method, in: Proceedings of the 54th AIAA Aviation Forum, Dallas, TX, USA, 2019.

[23] E. Alvarez, A. Ning, High-fidelity modeling of multirotor aerodynamic interactions for aircraft design, AIAA Journal 58 (10) (2020) 4385–4400.

[24] T. Stokkermans, D. Usai, T. Sinnige, V. LLM, Aerodynamic interaction effects between propellers in typical evtol vehicle configurations, Journal of Aircraft Article in Advance (2021) 1–19.

[25] J. B. Barlow, W. H. J. Rae, A. Pope, Low-Speed Wind Tunnel Testing, Third Ed., John Wiley and Sons, New York, 1999.

[26] H. Glauert, The Elements of Aerofoil and Airscrew Theory, Second Ed., University Press, Cambridge, 1948.

[27] M. Werle, Propeller wall blockage performance corrections, Journal of Propulsion and Power 27 (2) (2011) 496–498.

[28] M. Raffel, C. Willert, S. Wereley, J. Kompenhans, Particle image velocimetry — a practical guide, Springer, Berlin, 2007.

[29] A. Zanotti, M. Ermacora, G. Campanardi, G. G., Stereo particle image velocimetry measurements of perpendicular blade–vortex interaction over an oscillating airfoil, Experiments in Fluids 55 (2014) 1–13.

[30] F. De Gregorio, K. Pengel, K. K, A comprehensive piv measurement campaign on a fully equipped helicopter model, Experiments in Fluids 53 (2012) 37–49.

[31] G. Droandi, M. Syal, G. Bower, Analysis of the interactional aerodynamics of the vahana evtol using a medium fidelity open source tool, in: Proceedings of the VFS Aeromechanics for Advanced Vertical Flight Technical Meeting, AHS International, San Jose, CA, USA, 2020.

[32] S. Gallay, E. Laurendeau, Nonlinear generalized lifting-line coupling algorithms for pre/poststall flows, AIAA Journal 53 (7) (2015) 1784–1792.

[33] S. T. Piszkin, E. Levinsky, Nonlinear lifting line theory for predicting stalling instabilities on wings of moderate aspect ratio, Tech. rep., GENERAL DYNAMICS SAN DIEGO CA CONVAIR DIV (1976).

[34] L. Morino, C.-C. Kuot, Subsonic potential aerodynamics for complex configurations: a general theory, AIAA Journal 12 (2) (1974) 191–197.

[35] D. Montagnani, M. Tugnoli, F. Fonte, A. Zanotti, G. Droandi, M. Syal, Mid-fidelity analysis of unsteady interactional aerodynamics of complex

vtol configurations, in: 45^{th} European Rotorcraft Forum, Sept. 2019, Warsaw, Poland, 2019.

[36] A. Zanotti, A. Savino, M. Palazzi, M. Tugnoli, V. Muscarello, Assessment of a mid-fidelity numerical approach for the investigation of tiltrotor aerodynamics, Applied Sciences 11 (8) (2021) 3385.

[37] M. Drela, Xfoil: An analysis and design system for low reynolds number airfoils, in: T. J. Mueller (Ed.), Low Reynolds Number Aerodynamics, Springer Berlin Heidelberg, Berlin, Heidelberg, 1989, pp. 1–12.

[38] D. Althaus, Stuttgarter Profilkatalog: Meßergebnisse aus dem Laminarwindkanal des Instituts für Aerodynamik und Gasdynamik der Universität Stuttgart 1962-1972, no. v. 1, Institut fur Aerodynamik und Gasdynamik der Universitat.

[39] L. A. Viterna, D. C. Janetzke, Theoretical and experimental power from large horizontal-axis wind turbines, Tech. rep., Washington Procurement Operations Office, Washington, DC (United States) (Setptember 1982).

[40] D. Algarotti, Experimental-numerical investigation of the aerodynamic interaction between tandem propellers in evtol airplane mode, Master's thesis, Politecnico di Milano (2021).

[41] A. Zanotti, Experimental study of the aerodynamic interaction between side-by-side propellers in evtol airplane mode through stereoscopic particle image velocimetry, Aerospace 8 (9) (2021) 239.